HHS Public Access

Author manuscript

Structure. Author manuscript; available in PMC 2021 June 11.

Published in final edited form as:

Structure. 2019 November 05; 27(11): 1647–1659.e4. doi:10.1016/j.str.2019.08.009.

The Structural Basis of the Farnesylated and Methylated KRas4B Interaction with Calmodulin

Hyunbum Jang[1,6], **Avik Banerjee**[2], **Kendra Marcus**[3], **Lee Makowski**[3], **Carla Mattos**[3,6], **Vadim Gaponenko**[4,6], **Ruth Nussinov**[1,5,6,7,*]

[1]Computational Structural Biology Section, Basic Science Program, Frederick National Laboratory for Cancer Research, Frederick, MD 21702, USA

[2]Department of Chemistry, University of Illinois at Chicago, Chicago, IL 60607, USA

[3]Department of Chemistry and Chemical Biology, Northeastern University, Boston, MA 02115, USA

[4]Department of Biochemistry and Molecular Genetics, University of Illinois at Chicago, Chicago, IL 60607, USA

[5]Department of Human Molecular Genetics and Biochemistry, Sackler School of Medicine, Tel Aviv University, Tel Aviv 69978, Israel

[6]Senior author

[7]Lead Contact

SUMMARY

Ca^{2+}-calmodulin (CaM) extracts KRas4B from the plasma membrane, suggesting that KRas4B/CaM interaction plays a role in regulating Ras signaling. To gain mechanistic insight, we provide a computational model, supported by experimental structural data, of farnesylated/methylated $KRas4B_{1\text{-}185}$ interacting with CaM in solution and at anionic membranes including signaling lipids. Due to multiple interaction modes, we observe diverse conformational ensembles of the KRas4B-CaM complex. A highly populated conformation reveals the catalytic domain interacting with the N-lobe and the hypervariable region (HVR) wrapping around the linker with the farnesyl docking to the extended CaM's C-lobe pocket. Alternatively, KRas4B can interact with collapsed CaM with the farnesyl penetrating CaM's center. At anionic membranes, CaM interacts with the catalytic domain with large fluctuations, drawing the HVR. Signaling lipids establishing strong salt bridges with CaM prevent membrane departure. Membrane-interacting

*Correspondence: nussinor@mail.nih.gov.

AUTHOR CONTRIBUTIONS

H.J. and R.N. conceived and designed the study. H.J. conducted most of the simulations, analyzed the results, and wrote most of the paper. A.B. and V.G. conducted the NMR experiments, analyzed the results, and wrote the paper. K.M., L.M., and C.M. conducted the SAXS experiments, analyzed the results, and wrote the paper. All authors edited and approved the manuscript.

DECLARATION OF INTERESTS

The authors declare no competing interests.

SUPPLEMENTAL INFORMATION

Supplemental Information can be found online at https://doi.org/10.1016/j.str.2019.08.009.

KRas4B-CaM complex can productively recruit phosphatidylinositol 3-kinase α (PI3Kα) to the plasma membrane, serving as a coagent in activating PI3Kα/Akt signaling.

INTRODUCTION

Calmodulin (CaM) is a member of a family of calcium-binding proteins. It has 148 amino acid residues and consists of two symmetric globular domains, the N-lobe and the C-lobe, connected by a flexible central linker. CaM is a ubiquitous and highly versatile molecule involved in many physiological processes (Stevens, 1983). CaM can convert its conformation from a partially collapsed topology in the Ca^{2+}-free state (Komeiji et al., 2002) to a dumbbell-like, extended topology with four Ca^{2+} loaded to the EF-hand motifs (Babu et al., 1988). Although, there are more than 500 crystal structures currently available for CaM, and still more to come, no crystal data for the conformation of CaM in complex with KRas4B has been reported so far. Despite many efforts, it has been challenging to obtain the “exact” conformation of KRas4B-CaM by crystallization due to large fluctuations, stemming from the intrinsic, flexible nature of CaM’s central linker and the unfolded nature of the KRas4B hypervariable region (HVR, $KRas4B_{167\text{-}188}$). This results in several conformational ensembles for the KRas4B-CaM complex accommodating multiple conformations.

Recently, using explicit molecular dynamics (MD) simulations we provided possible modes of the interaction of CaM with the HVR peptide taken from the C-terminal tail of KRas4B (Jang et al., 2017). We used the chemical shift perturbation (CSP) data from NMR experiments (Abraham et al., 2009; Chavan et al., 2013) to guide initial constructions of the systems and presented atomistic models of the KRas4B HVR-CaM complex, illustrating that CaM stably binds to the farnesylated and methylated (FME) HVR with high affinity. The unfolded HVR is highly dynamic in the interaction with CaM, primarily targeting the CaM’s acidic linker with its polybasic anchor and docking to the hydrophobic pockets at both CaM’s lobes with the FME group. Isothermal titration calorimetry (Chavan et al., 2013) verified that electrostatic attraction alone between the central linker and the polybasic region is sufficient for the interaction (Erwin et al., 2016; Lopez-Alcala et al., 2008; Wu et al., 2011), while the hydrophobic interaction by the farnesyl docking to the pockets imparts stabilization of the complex. Our studies of the KRas4B HVR-CaM complex (Jang et al., 2017) revealed that CaM can adopt both extended and collapsed compact globular conformations in a dynamic assembly with KRas4B HVR via flexible-body motion.

It was reported that among the four KRas4A, KRas4B, NRas, and HRas isoforms (see sequences in Figure S1), CaM exclusively interacts with KRas4B (Abraham et al., 2009; Chavan et al., 2013; Jang et al., 2017; Villalonga et al., 2001; Wu et al., 2011), and can also bind KRas4A which also has a polybasic region (Nussinov et al., 2016b), extracting it from the membrane (Fivaz and Meyer, 2005; Sidhu et al., 2003; Sperlich et al., 2016). The absence of the interaction between CaM and other Ras isoforms, such as HRas and NRas, suggests that the interaction of CaM with Ras mainly involves the HVR, because the HVR significantly differs among Ras isoforms. That is, KRas4B HVR acts as a binding partner that is energetically favorable for CaM. Even though the CaM interaction with KRas4B

appears to be nucleotide-dependent with selective binding to the guanosine triphosphate (GTP)-bound KRas4B (Abraham et al., 2009; Chavan et al., 2013; Villalonga et al., 2001; Wu et al., 2011), the interaction can be nucleotide-independent with binding to both GTP- and guanosine diphosphate (GDP)-bound KRas4B (Agamasu et al., 2019; Fivaz and Meyer, 2005; Sidhu et al., 2003; Sperlich et al., 2016). To explain this apparent discrepancy, one can consider the accessibility of the HVR in different KRas4B conformational states. When GDP-bound, the catalytic domain sequesters the HVR, yielding an autoinhibited form of KRas4B in solution (Chavan et al., 2015; Lu et al., 2015). At the membrane, the HVR-induced autoinhibition may persist, burying the HVR in the interface between the catalytic domain and the membrane surface (Jang et al., 2016a). The autoinhibited KRas4B state is highly populated in the inactive GDP-bound state. However, there is also a minor species of the GDP-bound HVR-liberated state (Jang et al., 2016a; Nussinov et al., 2018b). CaM binding will shift the ensemble toward this HVR-accessible conformation, retaining the equilibrium among the states. The size of this population depends on the environment, which includes factors such as the solution, membrane composition, farnesyl insertion, and orientation/localization of the catalytic domain at the membrane. This suggests that CaM can bind to KRas4B even in the GDP-bound state when the HVR is in an accessible conformation.

Of particular interest is the functional role of the KRas4B-CaM complex in proliferative cell signaling. Two hypotheses have been put forward to explain the significance of Ca^{2+}-CaM in *KRAS*-driven cancer. In the first, KRas4B-specific binding to CaM reduces the number of CaM molecules available to activate Ca^{2+}-dependent protein kinase II (Wang et al., 2015), suppressing non-canonical WNT signaling pathway and consequently leading to β-catenin/T-cell factor activation (Nussinov et al., 2016c). In the second scenario, CaM is an integral component in the KRas4B interaction with phosphoinositide-3-kinase α (PI3Kα). PI3Kα produces phosphatidylinositol (3,4,5)-trisphosphate (PIP_3), which stimulates the PI3Kα/Akt/mammalian target of rapamycin pathway, regulating cell growth and survival, cytoskeleton reorganization, and metabolism (Castellano and Downward, 2011). Observations that CaM binds to PI3Kα activating it (Joyal et al., 1997; Wang et al., 2018; Zhang et al., 2017, 2018) and KRas4B is the only Ras isoform to bind CaM (Abraham et al., 2009; Chavan et al., 2013; Jang et al., 2017; Villalonga et al., 2001; Wu et al., 2011) suggest that CaM and KRas4B are key players in stimulating the PI3Kα/Akt pathway in adenocarcinoma cells with high calcium level (Sauter et al., 2015). This implicates the fundamental significance of CaM in *KRAS*-driven adenocarcinoma, which can constitute KRas4B-CaM complex a new drug discovery target.

Our previous model of the KRas4B HVR-CaM complex was constructed in the absence of the catalytic domain (Jang et al., 2017). To complete the picture of the interaction, we model the FME KRas4B-CaM complex. We test our models by explicit solvent MD simulations, and further confirm our results by NMR CSP and small-angle X-ray scattering (SAXS) data. We find the catalytic domain interaction with CaM, which appears weak and transient, as well as the strong HVR interaction, which drives the complex formation. In solution, the SAXS envelop highlights a populated conformation of the KRas4B-CaM complex, with the catalytic domain interacting with CaM's N-lobe and the HVR spans the extended central linker with the farnesyl docking to the C-lobe hydrophobic pocket, which is consistent with

the NMR and MD observations. However, because of the highly flexible nature of CaM's linker and the KRas4B HVR, we suggest multiple modes of interactions of CaM with KRas4B, presenting various conformational ensembles. CaM could extract KRas4B from the plasma membrane (Fivaz and Meyer, 2005; Sidhu et al., 2003; Sperlich et al., 2016), but signaling lipids such as phosphatidylinositol 4,5-bisphosphate (PIP_2) and phosphatidylinositol 5-phosphate (PI5P) can prevent KRas4B departure from the membrane. We suggest that the membrane-bound KRas4B-CaM complex can recruit PI3Kα to the plasma membrane and regulate PI3Kα activation. Our structural data provide possible conformational ensembles of the FME KRas4B-CaM complex in solution and at the membrane in atomic detail.

RESULTS

The Interaction of the KRas4B Catalytic Domain with CaM

To assist the computational modeling in addressing the question of how KRas4B interacts with CaM, we first identify those CaM residues involved in the interaction with KRas4B by tracing the CSPs on the CaM residues from our earlier studies (Abraham et al., 2009; Chavan et al., 2013). The most significant chemical shift changes induced by the catalytic domain $KRas4B_{1\text{-}166}$ occur in regions comprising the N-lobe (Thr5, Ile27, Thr28, Leu32, Ala57, and Glu67) and the C-lobe (Phe92, Arg106, Met109, and Asn111) of CaM. With full-length $KRas4B_{1\text{-}188}$, the chemical shift changes occur in the N-lobe (Ala15, Thr29, Leu32, Leu48, Ile52, and Glu67), the central linker (Asp78 and Thr79), and the C-lobe (Phe92, Arg106, Met109, Thr110, Asn111, Gln143, Met144, and Met145) of CaM. The significantly perturbed residues are mapped on two different crystal structures of CaM; one with a stretched linker and the other one with a collapsed linker (Figure 1A). The NMR CSP data illustrate that significant CSPs induced by the KRas4B catalytic domain are mainly observed in both lobes of CaM. The absence of CSPs in the linker region suggests that CaM's acidic linker mainly targets the polybasic KRas4B HVR (Abraham et al., 2009; Chavan et al., 2013; Jang et al., 2017). To classify KRas4B residues involved in the interaction with CaM, we next performed $^{1}H\text{-}^{15}N$ HSQC NMR spectra of $KRas4B_{1\text{-}188}$ in the GTP-γ-S bound state and compared the spectra of KRas4B titration with CaM. Spectral comparison reveals residues on KRas4B with significant CSPs caused by CaM (Figure 1B, left panel). These can indicate the binding sites and conformational rearrangements due to binding. Residues with significant CSPs are mapped on the KRas4B structure (Figure 1B, right panel). In the KRas4B catalytic domain, the chemical shift changes occur in the β1 (Glu3 and Tyr4), α1 (Leu23 and Gln25), L2 (Val29), β2 (Lys42 and Val45), β3 (Thr50 and Leu52), switch II (Asp69), L5 (Glu76), L6 (Asn86), α3 (Lys88 and Arg97), L8 (Thr124), and α5 (Asp154, Arg161, and Ile163) regions. We observed that the changes occur in many regions of the catalytic domain, implicating multiple binding modes. The CSP data for both the KRas4B and CaM residues were used in the initial construction of the KRas4B-CaM complex.

Although NMR CSPs provide the important residues from broad ensembles of the KRas4B-CaM interaction, detailed structural information for the molecular interaction is still unavailable. To obtain the ensembles of the interaction between the KRas4B catalytic

domain and CaM, we first used the Rosetta docking program (Kahraman et al., 2013; Sircar et al., 2010) to predict the molecular interaction for constructing initial structures for the MD simulation. In the molecular docking, we adopted two possible topologies of Ca^{2+}-CaM from crystal structures exhibiting stretched and collapsed central linkers. We generated multiple decoys of the KRas4B$_{1\text{-}166}$-CaM complex and collected the best representative decoys based on the energy score. We obtained 60 different decoys of the KRas4B$_{1\text{-}166}$-CaM complex with extended CaM (Figure S2). Another set of 60 decoys of the complex was obtained with collapsed CaM (Figure S3). To obtain the best configurations for MD simulations, we screened these based on the NMR CSPs, which provided hints for the interaction of the KRas4B catalytic domain with CaM (see the STAR Methods section for details). From the predicted decoys, we obtained eight different initial configurations of truncated KRas4B$_{1\text{-}166}$-CaM complex: four configurations (configs. 1–4) with extended CaM and four configurations (configs. 5–8) with collapsed CaM. We performed MD simulations on the KRas4B$_{1\text{-}166}$-CaM complexes in an aqueous environment. During the simulations, we observed that there is a significant conformational change from the initial conformation, while no immediate dissociation of CaM from the KRas4B catalytic domain was observed (Figure S4). Except for config. 6, large fluctuations in the interaction energy between the catalytic domain and CaM (Figure 2) indicate no specific binding mode of the molecular interaction, suggesting that their interactions are transient. The averaged interaction energies of KRas4B$_{1\text{-}166}$ with CaM over four configurations containing extended (configs. 1–4) and collapsed (configs. 5–8) CaMs are -193.3 ± 128.0 and -215.7 ± 61.0 kcal/mol, respectively. The absence of NMR CSPs on the CaM linker caused by the catalytic domain (Abraham et al., 2009; Chavan et al., 2013) suggests that the catalytic domain interacts with either lobe of CaM as in configs. 4, 5, 7, and 8, or both lobes of CaM at the same time as in configs. 3 and 6, but not with the CaM linker. Intermolecular residue-residue contact maps show that CaM in configs. 1 and 2 slightly involves its central linker in the interaction with the catalytic domain (Figure S5), which represents unfavorable complex conformations.

Post-translationally Modified KRas4B Can Secure the Interaction with CaM

Recently, we have demonstrated that the FME HVR peptide predominantly targets the acidic linker of CaM, stabilizing the interaction via docking its farnesyl group into the hydrophobic pockets of CaM's lobes (Jang et al., 2017). To provide a complete model of the interaction of KRas4B with CaM, we considered full-length KRas4B$_{1\text{-}185}$-GTP in complex with CaM. In the initial constructions, we adopted the conformations of the truncated KRas4B$_{1\text{-}166}$-CaM complex in configs. 1–8. The FME HVR was covalently connected to the catalytic domain, representing the post-translational modification of Cys185 at the C terminus of KRas4B. A total of eight initial configurations containing the extended (configs. 9–12) and collapsed (configs. 13–16) CaMs were subjected to explicit MD simulations. During the simulations, we observed that complexes with extended CaM undergo large conformational changes (Figure 3, upper panel), yielding relatively large values of root-mean-squared deviation (RMSD) with respect to their initial conformations, which are 7.6, 10.8, 19.3, and 21.5 Å for configs. 9–12, respectively. The large values of RMSD are mainly due to repositioning of CaM with respect to the catalytic domain of KRas4B. Remarkably, the complex with extended CaM converges into two distinct molecular topologies. In configs. 9

and 11, the molecular topology shows the catalytic domain interacting with the N-lobe of CaM, and the HVR wrapping around the acidic linker domain with the farnesyl docking to the hydrophobic pocket in the C-lobe of CaM. In contrast, configs. 10 and 12 exhibit the molecular topology with the catalytic domain interacting with both lobes of CaM at the same time, and the HVR wrapping around the acidic linker domain with the farnesyl docking to the hydrophobic pocket in either lobe of CaM. The former molecular topology resembles an “L”-shaped complex conformation that was suggested in previous studies (Abraham et al., 2009; Chavan et al., 2013). For collapsed CaM, while the complex in config. 13 shows large conformational changes, other complexes in configs. 14, 15, and 16 mostly retain their initial conformations (Figure 3, lower panel), yielding relatively small values of RMSD, which are 14.2, 5.1, 6.5, and 4.0 Å for configs. 13–16, respectively. These complexes share a similar molecular topology in which the catalytic domain resides next to CaM, and the HVR tail inserts into the core of CaM with the farnesyl sandwiched between the hydrophobic pockets from both lobes.

In the presence of HVR with the farnesyl, KRas4B secures the interaction with CaM, because the HVR with the farnesyl docking stably anchors to the core of CaM, which provides a robust hinge point. Compared with the interaction of the catalytic domain lacking the HVR with CaM, more residues contribute to intermolecular contacts due to the secure interaction (Figure 4). For all configurations, the HVR exhibits high probability to contact CaM. Almost all polybasic Lys residues at the anchor region of HVR (residues 175–180) participate in the interaction with CaM. As observed in our previous studies for the KRas4B HVR-CaM complex (Jang et al., 2017), the electrostatic interaction of HVR with CaM is a major driving force to stabilize the $KRas4B_{1\text{-}185}$-CaM complex (Figure S6). In addition to the HVR, the catalytic domain also participates in the interaction with CaM. For the catalytic domain, the most probable CaM contacts occur in the β2 (Val45), L3 (Asp47), β3 (Glu49 and Thr50), L7 (Glu107 and Asp108), α4 (Lys128, Gln131, Asp132, and Arg135 to Tyr137), β6 (Pro140 to Glu143), and α5 (Asp154, Tyr157, Thr158, Arg161, Lys165, and His166) regions. Among them, the highest-frequency residues are Asp47, Thr50, Asp108, Gln131, Asp132, Arg135, Asp154, Thr158, Arg161, Lys165, and His166. For CaM, high-frequency residues averaged over all configurations with high probability to contact KRas4B occur in the N-lobe (Gln8, Glu11, Ala15, Leu18, Ala46, Glu47, Asp50, Met51, Asn53 to Val55, and Glu67), the central linker region (Met71 to Ala88), and the C-lobe (Val91, Phe92, Asn111, Leu112, and Gln143 to Lys148). Among them, the highest-frequency residues are Glu11, Asp50, Asn53, Glu54, Val55, Met71, Arg74, Lys75, Asp78, Thr79, Ser81, Glu82, Glu83, Glu84, Ile85, Glu87, Ala88, Val91, Phe92, Leu112, Met145, Thr146, and Lys148. Some highest-frequency residues in both the KRas4B catalytic domain and CaM are also confirmed by significant NMR CSPs.

To quantify the interaction of KRas4B with CaM, we calculated separately the interaction energies of the KRas4B catalytic domain, HVR, and farnesyl group with CaM (Figure 5A). The averaged total interaction energies of $KRas4B_{1\text{-}185}$ with CaM over four configurations containing the extended (configs. 9–12) and collapsed (configs. 13–16) CaMs are −988.0 ± 89.8 and −1,088.7 ± 196.5 kcal/mol, respectively. These include the averaged interaction energies of the HVR, −792.8 ± 59.9 and −804.7 ± 138.4 kcal/mol for the extended and collapsed CaMs, respectively. These interaction energies are highly comparable with the

average interaction energy of ~1,000 kcal/mol for the KRas4B HVR-CaM complex (Jang et al., 2017), suggesting that, quantitatively, the HVR dominates the interaction with CaM. To quantify the conformations of the $KRas4B_{1-185}$-CaM complex, we calculated the binding free energy of the complex using molecular mechanics combined with the generalized Born (GB) and surface area continuum solvation (MMGBSA). We calculated the solvation free energy based on the GB employing the GBSW module (Im et al., 2003) of the CHARMM program (Brooks et al., 2009). We obtained the entropy contribution to the binding free energy from the principal moment of inertia combined with the quasiharmonic mode calculation in the VIBRAN module of the CHARMM program (Brooks et al., 2009). The number of vectors (mode) to calculate the vibrational analysis is set to NATOMX3, where NATOM denotes the number of atoms. Our calculations closely followed the protocol reported in previous studies (Jang et al., 2016b, 2017; Liao et al., 2018; Muratcioglu et al., 2017; Ozdemir et al., 2018a, 2018b; Zhang et al., 2017, 2018). In the calculations, we observed the lowest values of the binding free energy for configs. 10 and 11 with the extended CaM topology and for configs. 14 and 16 with the collapsed compact CaM topology (Figure 5B). These configurations illustrate that the catalytic domain strongly contributes to the binding free energy for the interaction (Figure 5A). Although these configurations can be designated as the most stable complex, they do not represent the highly populated ensembles of the complex conformation. Since the HVR mainly contributes to the interaction and the catalytic domain contributes only transiently, multiple modes of KRas4B-CaM association can be possible. Furthermore, the values of the binding free energy are rather similar for all configurations overlapping within their error range, suggesting that these are all possible ensembles of the complex conformations.

SAXS Data Unveil a Unique Molecular Topology for the KRas4B-CaM Complex

The MD studies provide a discrete set of conformational ensembles, because MD is unable to render all possible ensembles from the NMR observations owing to a lack of macroscopic samplings for the broad ensembles of the states. To render the highly populated conformation to further confirm our models, we obtained FME KRas4B from the Ras initiative team at the NCI (Gillette et al., 2015) and generated SAXS envelopes for the FME $KRas4B_{1-185}$-CaM complex, delineating the conformation of the complex. The envelope of the species was generated using *ab initio* methods provided by the DAMMIF package. A tri-lobed envelope was constructed from an average of 15 envelopes (Figure 6A). The reproducibility of these calculations is high, with a normalized spatial disparity (NSD) value less than 1 (NSD = 0.58 ± 0.03). The generated envelope from the SAXS data shows three major lobes within the envelope. The larger lobe represents the KRas4B catalytic domain, and the two smaller lobes represent an extended conformation of CaM, constituting the L-shaped molecular topology for the complex as observed in the MD studies. To retrieve the envelope for the structure, we confined the $KRas4B_{1-185}$-CaM complex into the SAXS envelop, generating three different SAXS models, SM-1, SM-2, and SM-3 (see the STAR Methods section for details). The theoretical scattering of the envelope was back calculated and compared with the experimental data, resulting in a $\chi^2 > 3$, with excellent fit to the data at low resolution and significant deviation in the high-resolution range (Figure 6B). The SAXS data were collected at two different concentrations, 5 and 10 mg/mL. Figure 6C plots the two datasets with error bars and Figure 6D shows the two datasets superimposed after

scaling the 5 mg/mL dataset by a factor of 2. This gives us confidence that the sample concentrations were measured correctly, and that aggregation is unlikely to be a contributing factor. The theoretical scattering curves of the models show much better fits extending to the higher-resolution data, as expected if the models reasonably represent the major species in solution. SM-l fits the experimental data with $\chi^2 = 2.14$ and SM-2 with $\chi^2 = 1.84$.

SM-3 is a hybrid model with the catalytic domain (residues 1–166) plus the HVR linker (residues 167–173) from SM-2, and the HVR anchor (residues 174–185) from previous simulations of the HVR-CaM complex (config. 1 of Jang et al., 2017) (Figure 7A). This hybrid model was based on good overlap between residues 173 and 175 upon superposition of the CaM structure in the two models. We observed that the alignment of the HVR in SM-2 and the simulated HVR occurs before the residues interact directly with the CaM linker (Figure S7). While the KRas4B catalytic domain resides in CaM's N-lobe, the HVR in the two models approaches CaM's C-lobe from the opposite sides of the linker, with the farnesyl group entering straight into the hydrophobic pocket in the C-lobe. SM-3 fits the SAXS data with $\chi^2 = 2.12$ (Figure 7B). Surprisingly, in terms of their χ^2 values, the best fit between the three models is SM-2 in which the farnesyl group is not bound in the hydrophobic pocket of CaM's C-lobe, but instead is positioned between the N- and C-lobes (Figure 6A). However, the fit is even better if the FME group is removed from SM-2, which lowers the χ^2 value to 1.76. This indicates that the FME group is unlikely to be positioned correctly in SM-2. Using the minimal ensemble search feature of the FoXS server (Pelikan et al., 2009; Schneidman-Duhovny et al., 2016), we found that a combined model with weighted functions of 75% contribution from SM-2 and 25% contribution from SM-3 lowered the overall χ^2 value of the fit to 1.69. Removing the farnesyl modification from SM-2 further lowered the χ^2 value of this balance to 1.65. These results support a highly dynamic complex that may sample conformations represented in both models, although the question of which side the HVR enters to interact with the C-terminal lobe is left unresolved due to the low resolution of the data.

CaM Interaction with KRas4B at the Anionic Lipid Bilayers Implicating Membrane Extraction

We previously demonstrated that CaM extracted the FME HVR peptide from the phospholipid bilayers (Jang et al., 2017). To monitor how CaM attacks KRas4B at the membranes, we further performed all-atom MD simulations on the $KRas4B_{1\text{-}185}$-CaM complex at the membranes. Four different types of the anionic lipid bilayers, DOPC:DOPS, DOPC:DOPS:DOPA, DOPC:DOPS:7PIP_2, and DOPC:DOPS:PI5P bilayers were employed in the simulations. The double-composition bilayer (hereafter referred to PS bilayer) has a molar ratio 4:1, and all triple-composition bilayers (PA, PIP_2, and PI5P bilayers) have the same molar ratio of 32:7:1. To observe the efficiency of lipid composition-dependent action of CaM, we used the same initial membrane-anchored $KRas4B_{1\text{-}185}$-GTP conformation that was taken from previous studies (config. 1 of Jang et al., 2016a). At the starting point, extended CaM was located next to KRas4B, with its linker facing the HVR. The farnesyl was pre-inserted into the bilayer, and no direct contacts between the CaM linker and the polybasic HVR were assigned. Remarkably, during the simulations we observed that CaM continuously wrestles with the KRas4B catalytic domain, pushing it to intercept the HVR

underneath it (Figure 8A). In the PS and PA bilayers, CaM constantly pursues the HVR to pull out the anchor portion including the farnesyl. However, we did not observe complete removal of the HVR from the bilayer due to a limited simulation timescale. We anticipate that CaM eventually shifts the equilibrium toward successful extraction of the HVR from the anionic bilayers and leaves the membrane (Fivaz and Meyer, 2005; Sidhu et al., 2003; Sperlich et al., 2016). In the PIP_2 and PI5P bilayers with signaling lipids, CaM significantly overturns the KRas4B catalytic domain. This action is efficient, with CaM easily snatching the polybasic HVR using its acidic linker, while confining the catalytic domain to the membrane surface. We observed that CaM extracts the HVR from PIP_2 and PI5P bilayers slightly better than from PS and PA bilayers (Figure 8B). In the PI5P bilayer, the farnesyl is almost extracted to the nearby bilayer surface. Notably, the farnesyl insertion is highly reversible due to the *cis* conformation in the unsaturated carbon chain (Nussinov et al., 2016b), suggesting that it can be populated either in the hydrophobic core of the bilayer or on the bilayer surface.

Interestingly, CaM is involved in strong salt bridge interactions with the signaling lipids, PIP_2 and PI5P. In the PIP_2 bilayer, the CaM residues, Arg90 and Lys94, participate in salt bridge interactions with PIP_2, and Lys115 forms a salt bridge with DOPS (Figure 9A). In the PI5P bilayer, Lys115 interacts with PI5P through a salt bridge (Figure 9B). However, we did not observe any salt bridge interaction of CaM with anionic lipids in bilayers containing only DOPS and DOPA. This suggests that the signaling lipids promote the interaction of CaM with the anionic bilayers. The salt bridge may provide a pivot point that allows CaM to draw efficiently the HVR from the anionic bilayers. The HVR also coordinates with the signaling lipids; two PIP_2 and one PI5P interact with the HVR during the simulations (Figure S8).

DISCUSSION

Here, we decipher an unsolved structural mystery of the KRas4B interaction with Ca^{2+}-CaM using explicit MD simulations, NMR CSPs, and SAXS experiments. The initial models for the KRas4B catalytic domain interacting with CaM were compared with structural data from the NMR experiments (Abraham et al., 2009; Chavan et al., 2013). We observe that the interaction of the catalytic domain on its own with CaM is weak and highly transient. The binding interface in the $KRas4B_{1\text{-}166}$-CaM complex appears to be highly dynamic, suggesting that multiple modes of the complex conformation are possible. This is in line with the lack of crystal data for the conformation of the KRas4B-CaM complex. When CaM interacts with C-terminal truncated KRas4B, the significantly perturbed residues on CaM can be found in both N- and C-lobes of CaM, but not in its central linker. This indicates that CaM preserves its acidic linker for the polybasic KRas4B HVR.

FME $KRas4B_{1\text{-}185}$ secures the interaction with CaM via strong electrostatic attraction between the HVR and CaM, which is consistent with our earlier observations (Chavan et al., 2013; Jang et al., 2017). The farnesyl docking to the hydrophobic pockets located in either of CaM's lobes imparts stabilization of the $KRas4B_{1\text{-}185}$-CaM complex. In the complex, the HVR is dominant in the interaction with CaM compared with the catalytic domain, suggesting that the HVR should lead to formation of the complex. When the polybasic HVR

interacts with the acidic linker, the farnesyl tail can dock into either lobe of CaM. This determines the location of the catalytic domain that interacts with CaM's lobe, yielding distinct molecular topologies of the complex. For the complex with extended CaM, the catalytic domain mainly resides next to CaM's N-lobe, exhibiting the L-shaped molecular topology of the complex. In this topology, the farnesyl docks to the C-lobe hydrophobic pocket. The L-shaped topology was suggested in previous NMR studies (Abraham et al., 2009; Chavan et al., 2013) and verified by the current MD simulations and SAXS experiments. However, we also observe that the catalytic domain interacts with both lobes of the extended CaM at the same time as seen in config. 10. This molecular topology of the complex can explain why the significantly perturbed residues are also found in the C-lobe of CaM. We speculate that concurrent interactions of both lobes with the catalytic domain can induce flexibility in the central linker, promoting a compact conformation of CaM. The complex with collapsed CaM yields a unique topology, with the farnesyl penetrating the center of CaM and the catalytic domain extending from the edge of the HVR linker. In this topology, the farnesyl is sandwiched between the hydrophobic pockets from both lobes, and the adjacent catalytic domain interacts with both lobes at the same time. Because CaM presents variable conformations owing to the flexible linker, it is possible that CaM can collapse and wrap around the farnesylated HVR. It has been observed that a lipidated peptide modified with myristoyl in complex with the collapsed CaM is an unstructured, non-helical motif (Matsubara et al., 2004), as the KRas4B HVR.

It is very difficult to predict the exact conformations of CaM when it interacts with binding partners. CaM is most often in the collapsed conformation when bound to α-helical peptides (Gifford et al., 2012; Meador et al., 1992; Yamauchi et al., 2003). Alternatively, CaM also adopts an extended conformation in complex with binding proteins (Deng et al., 2013; Killock et al., 2009; Lopez-Alcala et al., 2008). Here, we provide possible modes of the interaction of KRas4B with both the extended and collapsed CaMs in atomic detail. When Ca^{2+} is loaded to the EF hands, CaM (Holo-CaM) adopts an extended dumbbell-like shape (Babu et al., 1988). Without binding partners, the extended CaM should be populated in solution. Thus, the extended CaM first recognizes a membrane-anchored KRas4B as a binding target (Figure 10). At the membrane, CaM attracts the KRas4B HVR through strong electrostatic interactions, ultimately detaching the HVR and the farnesyl tail from the membrane. Depending on the lipid compositions, CaM can successfully extract KRas4B from the membrane, translocating it to the endomembrane. In the cytosol, the fluctuations determine the conformation of the membrane-unbound KRas4B-CaM complex, shifting the equilibrium to the L-shaped molecular topology of the complex. However, phosphatidylinositol lipids can prevent the departure of KRas4B through direct interactions with CaM and the HVR. It was reported that PIP_2 can stably bind to CaM in complex SK channels at the membrane (Logothetis et al., 2015; Zhang et al., 2014).

Ras predominantly exists as dimers or nanoclusters (Nussinov et al., 2019a, 2019b), and Raf activation requires Ras nanoclustering. However, PI3K activation does not require Ras nanoclusters; Ras monomers can activate PI3K (Nussinov et al., 2019a). CaM can isolate Ras from nanoclusters. Here, we propose that the membrane-bound KRas4B-CaM complex can contribute to two independent mechanisms in PI3Kα activation (Figure 10). We speculate that, under physiological conditions, CaM can deliver KRas4B to PI3Kα, which is

activated by binding to the phosphorylated C-terminal tyrosine motif (pYxxM) in receptor tyrosine kinase (RTK). PI3Kα is activated by stimulated RTK, which can release the inhibitory N- and C-terminal Src homology 2 (SH2) domains from the catalytic subunit. The high-affinity interaction of the SH2 domains with the phosphorylated tyrosine motif disrupts the p85α-p110α subunit interactions in PI3Kα (Nolte et al., 1996; Pauptit et al., 2001). It was observed that nSH2 release is a prerequisite for PI3Kα activation (Joyal et al., 1997; Yu et al., 1998; Zhang et al., 2019a, 2019b). PI3Kα is fully activated by RTK and Ras, which stabilizes PI3Kα at the membrane in a catalytically productive state. In adenocarcinoma of *KRAS*-driven cancer (Nussinov et al., 2015, 2016a), both CaM and KRas4B play a role in stimulating PI3Kα/Akt signaling (Liao et al., 2006; Nussinov et al., 2015, 2016a, 2016c, 2018a). In the absence of RTK, Ca^{2+}-CaM can also deliver KRas4B to RTK-independent, activated PI3Kα. Early evidence pointed to the direct interaction of CaM with the SH2 domains (Joyal et al., 1997), followed by recent observations that phosphorylated CaM at Tyr99 binds the nSH2 domain (Zhang et al., 2017), replacing the missing RTK signal (Wang et al., 2018; Zhang et al., 2017, 2018). PI3Kα can be activated by pCaM, which interacts with the nSH2 domain of the p85α subunit, releasing autoinhibition on the p110α subunit (Zhang et al., 2019a, 2019b). Membrane-attached CaM by phosphatidylinositol lipid sequesters the cSH2 domain reducing the fluctuations (Joyal et al., 1997; Wang et al., 2018; Zhang et al., 2018). Finally, KRas4B stabilizes PI3Kα at the membrane at a favored orientation, fully activating it. Notably, in KRas4B-driven pancreatic cancer epidermal growth factor receptor is often overexpressed (Lemoine et al., 1992; Oliveira-Cunha et al., 2011), particularly in late stages, resulting in a higher population of stimulated receptors, which may obviate or collaborate with pCaM in PI3Kα activation.

Detailed structural information of KRas4B in complex with CaM is useful to understand the mechanism of KRas4B regulation of the PI3Kα/Akt pathway. We envision that, by shifting the conformational equilibrium, CaM can “extract” KRas4B from the membrane (Fivaz and Meyer, 2005; Sidhu et al., 2003; Sperlich et al., 2016), or possibly recruit KRas4B to the plasma membrane with a role similar to the delta subunit of the cGMP phosphodiesterase from retinal rod cells (PDEδ). PDEδ targets the farnesyl group of Ras proteins in a nucleotide-independent manner (Chandra et al., 2011; Muratcioglu et al., 2017) and is involved in Ras delivery to the plasma membrane (Schmick et al., 2014; Weise et al., 2012).

To conclude, we combine comprehensive experimental techniques of NMR CSPs and SAXS envelops with atomistic simulation to obtain realistic conformations of the KRas4B-CaM complex and propose its functional role in connection with PI3Kα in cell proliferation. We present multiple modes of the interaction of KRas4B in complex with CaM. In solution, the KRas4B-CaM conformation is highly fluctuating, visiting different conformational ensembles depending on CaM’s conformational states. The highly populated ensembles reveal that the catalytic domain interacts with the N-lobe and the farnesyl docks to the C-lobe hydrophobic pocket of the extended CaM, yielding the L-shaped molecular topology. Our structural data provide detailed information on how CaM assembles to form a complex with KRas4B, and how it targets the polybasic HVR-accessible conformation facilitating the KRas4B extraction from the membrane. Understanding the role of CaM at the membrane in conjunction with the PI3Kα/Akt pathway is crucial for providing a putative drug discovery

target in PI3K activation by oncogenic KRas4B. Recently our detailed simulations also proposed a PI3Kα isoform-specific putative drug pocket (Zhang et al., 2019a, 2019b).

STAR★METHODS

LEAD CONTACT AND MATERIALS AVAILABILITY

Further information and requests for resources and reagents should be directed to and will be fulfilled by the Lead Contact, Ruth Nussinov (NussinoR@mail.nih.gov).

EXPERIMENTAL MODEL AND SUBJECT DETAILS

Both pRSF1b-RalA and pET15b-CaM were expressed in in BL21(DE3) cells.

METHOD DETAILS

NMR ^{1}H-^{15}N HSQC—The ^{1}H-^{15}N heteronuclear single quantum coherence (HSQC) NMR experiments were performed on a 900 MHz Avance Spectrometer (Bruker Biospin, Billerica, MA) equipped with a cryogenic probe. All experiments were carried out at 25°C. The buffer conditions were as follows: 10% D_2O, 50 mM Tris-Citrate (pH 6.5), 50 mM NaCl, 5 mM $MgCl_2$, 20 mM $CaCl_2$ and 2 mM β-mercaptoethanol. Two-dimensional ^{1}H-^{15}N HSQC spectra of ^{15}N $KRas4B_{1\text{-}188}$ were acquired at a protein concentration of 100 μM in the absence or presence of the unlabeled CaM at a molar ratio 1:1.

For $KRas4B_{1\text{-}188}$, the HSQC peaks were identified according to the NMR assignments published before (Abraham et al., 2009; Chavan et al., 2013). NMR data were processed with NMRPipe (Delaglio et al., 1995). The observed amide resonance chemical shift perturbations were calculated using the equation as we have done previously (Abraham et al., 2009; Chavan et al., 2013),

$$\Delta\delta_{NH} = \sqrt{\frac{(\Delta\delta_H)^2 + (\Delta\delta_N)^2 / 25}{2}}, \quad \text{(Equation 1)}$$

where $\Delta\delta_H$ and $\Delta\delta_N$ are the observed chemical shift changes for ^{1}H and ^{15}N. The chemical shift changes above average plus one standard deviation were considered statistically significant, as commonly done in NMR studies.

Generating Initial Configurations of KRas4B-CaM Complex for Explicit MD Simulations—We used the Rosetta docking program (Kahraman et al., 2013; Sircar et al., 2010) to generate initial configurations of KRas4B-CaM. The crystal structure of KRas4B catalytic domain (PDB code: 3GFT, residues 1-166) was docked to two Ca^{2+}-loaded CaM crystal structures (PDB codes: 1CLL (Chattopadhyaya et al., 1992) and 1CDL (Meador et al., 1992)). The KRas4B is GppNHp (a GTP analog)-loaded, with a point mutation Q61H, which was converted to wild-type. For CaMs, 1CLL is an isolated CaM with an extended linker, and 1CDL is a collapsed CaM with a flexible linker. The compact globular CaM contains a binding partner, known as a CaM binding α-chain domain (residues 1731-1749) from myosin light chain kinase (MYLK), smooth muscle. Multiple decoys were generated to

predict the KRas4B catalytic domain interaction with CaM by the Rosetta docking program (Kahraman et al., 2013; Sircar et al., 2010). Initially, we collected 60 decoys based on the energy score for each conformation of CaM and then screened these based on the NMR CSP data. We counted residue contacts for both the KRas4B and CaM residues with significant CSPs involved in the interaction. We further ensured that the initial configurations are feasible for implementing the full-length simulations by checking whether the farnesyl group in the HVR tail is able to dock into the hydrophobic pockets of either lobes of CaM. An example of such catalytic domain orientation shows that for the decoy #6 with the extended CaM, the farnesyl is unreachable to the hydrophobic pockets due the limited length of the HVR. The farnesyl docking is a prerequisite for the KRas4B–CaM interaction (Abraham et al., 2009; Chavan et al., 2013; Jang et al., 2017). For each conformation of CaM, we selected initial configurations of $KRas4B_{1\text{-}166}$–CaM complex; four configurations (Configs. 1-4) with the extended CaM and four configurations (Configs. 5-8) with the collapsed CaM. Further to represent FME $KRas4B_{1\text{-}185}$ interacting with CaM, the HVR was constructed for Configs. 1-8 to model $KRas4B_{1\text{-}185}$-CaM complex. A total of eight initial configurations of the complex with the extended CaM (Configs. 9-12) and collapsed CaM (Configs. 13-16) were generated. In KRas4B HVR, the Cys-185 residue was modified with both farnesylation and methylation. The tail of the farnesyl group initially faced either hydrophobic pockets in both CaM's lobes.

Atomistic Molecular Dynamics Simulations—A total of sixteen initial configurations were subject to the MD simulations in aqueous environment; $KRas4B_{1\text{-}166}$ interacting with four extended and four collapsed CaMs and FME $KRas4B_{1\text{-}185}$ interacting with four extended and four collapsed CaMs. In addition to these, four simulations were performed for FME $KRas4B_{1\text{-}185}$ interacting with the extended CaM at the membranes, composed of four different types of anionic lipid bilayers; DOPC:DOPS (molar ratio 4:1), DOPC:DOPS:DOPA (molar ratio 32:7:1), DOPC:DOPS: PIP_2 (molar ratio 32:7:1), and DOPC:DOPS:PI5P (molar ratio 32:7:1). We used the membrane-anchored $KRas4B_{1\text{-}185}$-GTP conformation from previous studies (Jang et al., 2016a) in the initial construction at the membrane.

Our simulations closely followed the same protocol as in our previous works (Chavan et al., 2015; Jang et al., 2015; Jang et al., 2017; Jang et al., 2016a; Jang et al., 2016b; Liao et al., 2018; Lu et al., 2015; Lu et al., 2016; Muratcioglu et al., 2017; Ozdemir et al., 2018a; 2018b; Zhang et al., 2017; Zhang et al., 2019a, 2019b; Zhang et al., 2018). The solution simulations were performed with the modified TIP3P water model that constitutes the isometric unit cell box containing the complex. Na^+ and Cl^- were added, to neutralize system, but also to satisfy a total ion concentration near 100 mM. We employed the updated CHARMM all-atom additive force field (Brooks et al., 2009) (version C36) for constructing the set of starting points and relaxing the systems to a production-ready stage. The anionic lipid bilayers were generated using the bilayer building protocol as described in our previous publications (Jang et al., 2015, 2016a, 2016b). A series of minimization cycles were performed for the solvents around the harmonically restrained protein complex. The pre-equilibrium simulations for 2 ns were performed on each configuration system with the restrained backbones of KRas4B and CaM until the solvent reached 310 K. At the final pre-

equilibrium stage, the harmonic restraints on the backbones of KRas4B and CaM were gradually removed through dynamic cycles with the full Ewald electrostatics calculation. This ensured that the protein complex adapts to the surrounding heat bath. The production runs were performed with the Langevin temperature control that maintains the constant temperature at 310 K and the Nosé-Hoover Langevin piston pressure control that sustains the pressure at 1 atm. Each independent simulation was performed for 1 μs, which gives rise to a total of 20 μs simulations. The NAMD parallel-computing code (Phillips et al., 2005) on a Biowulf cluster at the National Institutes of Health (Bethesda, MD) was employed for the production runs.

Expression and Purification of CaM—The cDNA for Chicken CaM (amino acid sequence identical to that of human CaM) provided by Prof. Joshua Wand was inserted into the pET15b vector. CaM was expressed in BL21(DE3) cells co-transformed with the pRSF1b-RalA and pET15b-CaM vectors so that the two proteins were expressed simultaneously. This was done to enhance the RalA yield in the soluble fraction in experiments originally used to study the RalA/CaM interaction. Glycerol stocks were stored at −80°C.

For the expression and purification of CaM, a 200 mL culture of BL21 cells with both the RalA and CaM expressing plasmids was grown overnight at 37°C in LB broth containing ampicillin (50 mg/L) and kanamycin (36 mg/L), with shaking at 225 rpm. This overnight culture was used to inoculate six Erlenmeyer flasks containing 1 L of LB broth (30 mL culture/1 L LB broth). The fresh cultures were grown at 37°C with shaking for 2-3 hours, until the OD_{600} reached 0.600-0.800. Protein expression was induced with 1 mM IPTG and allowed to grow for 3-5 hours at 30°C. The cell pellet was harvested by centrifugation at 9000 rpm for 20 min. Atypical cell pellet yield was around 13-20 grams, stored at −80°C.

The frozen cell pellet was suspended in 50 mL of low salt buffer (20 mM HEPES pH 7.5, 50 mM NaCl, 5 $MgCl_2$, 0.1 mM EGTA, 1 mM DTT, 20 μM GDP, and 2% glycerol) in the presence of protease inhibitors (2 μg/mL antipain, 1 μg/mL leupeptin and 1 μ/mL pepstatin A). Resuspension took about 1-2 hours on ice. The cells were sonicated on ice for a total of 5 min in cycles of 30 seconds at 15 mV and 30 seconds pauses. The lysed cells were centrifuged for 30 min at 15,000 rpm at 4 °C. The soluble fraction was pooled on ice and filtered through 0.45 micrometer filters. The filtered lysate was loaded into a 150 mL super loop and subjected to separation on a Hi Prep QFF column using a 0-40% gradient of high salt buffer (identical to the low salt buffer but containing 1 M NaCl). Fractions containing CaM were identified by SDS-PAGE and pooled on ice. The remaining fractions were discarded. CaM was further purified via hydrophobic interaction chromatography (HIC). Calcium chloride was added to the pooled CaM fractions to 15 mM prior to loading into a 150 mL superloop (20-30 mL of protein solution). A HiPrep Phenyl FF was equilibrated with CaM buffer A (50 mM HEPES pH 7.5 and 1 mM $CaCl_2$) prior to protein injection. After the injection of CaM, the column was washed first with CaM buffer A and then with CaM buffer B (same as CaM buffer A containing 0.5 M NaCl), and then CaM buffer A again. Elution of purified CaM occurred during a 0-100% gradient of CaM elution buffer (50 mM HEPES pH 7.5, 10 mM EGTA). Fractions containing purified CaM were identified via SDS-PAGE, pooled on ice and $CaCl_2$ was added to 15 mM to improve CaM stability. The

CaM yield was typically 60-100 mg. The protein was concentrated to about 10 mg/mL, flash-frozen and stored at −80°C in 100 μL aliquots.

SAXS Data Collection and Analysis—Purified FME KRas4B bound to the GTP analogue GppNHp was provided by the NCI Ras initiative team (Gillette et al., 2015). The concentrations of CaM and KRas4B were determined via the Bradford assay, the two proteins were combined on ice in a 1:1 molar ratio and the solution diluted to 5 mL with dialysis buffer (20 mM HEPES pH 7.0, 25 mM NaCl, 1 mM $CaCl_2$, 1 mM $MgCl_2$ and 1mM DTE). The complex solution was then dialyzed overnight (18 hours) at 4°C with stirring and concentrated via centrifugation to either 5 mg/mL or 10 mg/mL. We collected data at 5 mg/mL and 10 mg/mL and detected no significant differences in the data or the resulting envelopes. The samples were held for 1-2 days at 4°C prior to SAXS data collection.

SAXS data on the KRas4B-GppNHp–CaM complex at concentrations of 5 mg/mL and 10 mg/mL were collected at the Cornell High Energy Synchrotron Source (CHESS) at Cornell University (Ithaca, NY). Five 2s frames of data were combined (10s total exposure time) and buffer subtracted against five 2s frames corresponding to scattering of buffer alone. The ATSAS program package was used for all SAXS data analysis, including Guinier and Distance Distribution analysis, and molecular envelope construction.

The scattering average reconstruction envelope was visualized using two programs: PyMOL (DeLano, 2002) and Chimera (Pettersen et al., 2004). To generate the envelope surface in PyMOL, the dummy atoms within the envelope are visualized as spheres (sphere radius of 2.5 Å). The surface of the sphere model is then rendered with a solvent radius of 3 Å. In Chimera, the surface of the dummy atom model is rendered with the ‘molmap’ command with a resolution of 15 Å.

Construction of SAXS Models for FME KRas4B–CaM Complex—The KRas4B–PDEδ crystal structure (PDB code: 5TAR) (Dharmaiah et al., 2016) was selected to provide coordinates for the KRas4B HVR group. Water molecules, GDP, and the PDEδ were removed from the coordinate file and the remaining KRas4B was manually fit into the PyMOL rendering of the SAXS envelope, which contains a large spherical lobe that nicely fits the KRas4B catalytic domain and two smaller lobes that we associate with the N- and C-lobes of CaM connected by the linker region. This envelope supports the extended conformation of Ca^{2+}-CaM (PDB code: 3CLN) (Babu et al., 1988).

Since the catalytic domain in the complex with PDEδ (Dharmaiah et al., 2016) is bound to GDP, the crystal structure of $KRas4B_{1\text{-}166}$ bound to $GppCH_2p$ (PDB code: 5UK9) (Parker et al., 2018) was aligned with the catalytic domain from 5TAR to appropriately model the active KRas4B state. Residues 1-166 were then removed from the coordinates with 5TAR, creating a hybrid model of the catalytic domain of KRas4B-$GppCH_2p$ from 5UK9 and the HVR coordinates from 5TAR. The $GppCH_2p$ was replaced with GTP. This model, containing the farnesyl group, was manually docked onto the CaM structure in the extended conformation (PDB code: 3CLN) guided in part by previously published NMR chemical shifts (Abraham et al., 2009) and by visual fit to the SAXS envelop, which helped determine the angle between the extended CaM molecule and the KRas4B catalytic domain. In this

model, referred to as SAXS model 1 (SM-1), the farnesyl group interacts with the CaM C-lobe outside of the hydrophobic core, and the N-lobe interacts with residues in the catalytic domain. SM-1 was subjected to a mild annealing protocol to relieve clashes, using NAMD (Phillips et al., 2005) with the CHARMM all-atom additive force field (37). The model was solvated in a water box large enough so that no protein atom is less than 10 Å from the edge of the box and ionized to a final concentration of 0.15 M NaCl. The simulation was slowly heated from 100 K to 500 K in a stepwise manner and then cooled down to 100 K in an identical number of steps. The final frame of this simulation was taken as SM-2.

In order to position the farnesyl group in the C-lobe hydrophobic core, eight previously published KRas4B HVR–CaM models (Jang et al., 2017) were aligned with the CaM structure in both SM-1 and SM-2. Configuration 1 of the HVR–CaM model (Jang et al., 2017) was selected for modeling the farnesyl group based on the observation that the HVR in this simulation model overlapped well with that of SM-2 once the CaM structures in the two models were superimposed (Figure S7). Residues 173-175 of the HVR were particularly well aligned in SM-2 and the Configuration 1 of the HVR–CaM structure (Jang et al., 2017). Thus, the CaM coordinates and residues 174 through the C-terminal end of KRas4B were deleted from SM-2 and replaced by the HVR–CaM coordinates of Configuration 1 (Jang et al., 2017) from the simulations, resulting in SM-3. This hybrid model, with the KRas4B catalytic domain bound to GTP and the HVR–CaM from Configuration 1 (Jang et al., 2017) oriented by the overlap of HVR residues 173-175, showed an excellent visual fit to the SAXS envelope.

While a manual fit to the SAXS envelope was used to guide the construction of the HVR–CaM models, the final models were computationally fit to the SAXS envelope using Chimera (Pettersen et al., 2004), which places the model within a mesh representation of the scattering envelope. The envelope rendering, and fit of the protein models, were performed using the “fit” function of the mol map program. Through this process, bias of the envelope fit carried over through a manual process is minimized.

Fit between Model Theoretical Scattering Curves and Experimental Data Using FOXS-MES—The models described above were subjected to analysis using the programs FoXS and MultiFoXS (Pelikan et al., 2009; Schneidman-Duhovny et al., 2016). Simply put, a theoretical SAXS scattering curve is calculated from a set of PDB coordinates and compared to the experimental scattering. The fit between these two curves is measured as a χ^2 value, where the lower the value, the better the agreement between the theoretical and experimental curves. In general, we consider a χ^2 of 1 or less to be excellent, 1-2 is okay, above 2 is not good (Rodi et al., 2007). The MES (multiple ensemble scattering) capabilities of MultiFoXS can optimize the weight of multiple models to produce a best fit of a theoretical scattering curve to experimental data in the case of a flexible protein sampling multiple conformations. Of the single SM-1,2, and 3, the lowest scoring complex structure is that of represented by SM-2. However, a mix of SM-2 and SM-3 in a ratio of 75%:25% weighing functions provides the best χ^2 value, consistent with more than one conformational state in solution.

QUANTIFICATION AND STATISTICAL ANALYSIS

In analysis of the MD simulation trajectories, the first 100 ns trajectories of initial transients were removed, and thus averages were taken afterward. The same CHARMM programming package (Brooks et al., 2009) as used in the initial construction was employed for analyzing the simulated trajectories. The CAHRMM program (Brooks et al., 2009) calculated the interaction energy of KRas4B with CaM. In the binding free energy calculation using molecular mechanics combined with the generalized Born (GB) and surface area continuum solvation (MMGBSA), the solvation free energy was calculated by the GB using the GBSW module (Im et al., 2003) of the CHARMM program (Brooks et al., 2009).

DATA AND CODE AVAILABILITY

The accession numbers for the atomic coordinates and structure factors reported in this paper are PDB: 1CLL (CaM), 1CDL (CaM), 3CLN (CaM), 3GFT (KRas4B), 5TARx (KRas4B), 5UK9 (KRas4B).

Supplementary Material

Refer to Web version on PubMed Central for supplementary material.

ACKNOWLEDGMENTS

All simulations had been performed using the high-performance computational facilities of the Biowulf PC/Linux cluster at the National Institutes of Health (NIH), Bethesda, MD (https://hpc.nih.gov/). This project has been funded in whole or in part with federal funds from the National Cancer Institute (NCI), NIH, under contract HHSN26120080001E. The content of this publication does not necessarily reflect the views or policies of the Department of Health and Human Services, nor does mention of trade names, commercial products, or organizations imply endorsement by the US Government. This Research was supported (in part) by the Intramural Research Program of the NIH, NCI, Center for Cancer Research. The NMR experiment and analysis work were supported by the NCI grant R01 5R01CA188427-04 to V.G. The SAXS data collection and analysis work were supported by National Science Foundation (NSF) grant MCB-1517295 to C.M. The authors gratefully acknowledge the support from the Horizon Award fellowship (Department of Defense) under the congressionally approved medical research program (CDMRP) with grant no. W81XWH-17-1-0509 to A.B. Thanks to Andrew Stephan and his team at the NCI Ras initiative for providing the FME KRas4B-GppNHp used in the SAXS experiments. SAXS data were collected at the Cornell High Energy Synchrotron Source (CHESS). CHESS is supported by the NSF and NIH/National Institute of General Medical Sciences (NIGMS) via NSF award DMR-1332208, and the Macromolecular X-ray science at the CHESS (MacCHESS) resource is supported by NIH/NIGMS award GM-103485. We thank Jenifer Winters and Hao Zhou for help with the SAXS data collection at CHESS. Thanks to Nathan I. Nicely for developing the protocol for co-expression of Ral and CaM used to purify CaM for the SAXS experiments.

REFERENCES

Abraham SJ, Nolet RP, Calvert RJ, Anderson LM, and Gaponenko V (2009). The hypervariable region of K-Ras4B is responsible for its specific interactions with calmodulin. Biochemistry 48, 7575–7583. [PubMed: 19583261]

Agamasu C, Ghirlando R, Taylor T, Messing S, Tran TH, Bindu L, Tonelli M, Nissley DV, McCormick F, and Stephen AG (2019). KRAS prenylation is required for bivalent binding with calmodulin in a nucleotide-independent manner. Biophys. J 116, 1049–1063. [PubMed: 30846362]

Babu YS, Bugg CE, and Cook WJ (1988). Structure of calmodulin refined at 2.2 A resolution. J. Mol. Biol 204, 191–204. [PubMed: 3145979]

Brooks BR, Brooks CL 3rd, Mackerell AD Jr., Nilsson L, Petrella RJ, Roux B, Won Y, Archontis G, Bartels C, Boresch S, et al. (2009). CHARMM: the biomolecular simulation program. J. Comput. Chem 30, 1545–1614. [PubMed: 19444816]

Castellano E, and Downward J (2011). RAS interaction with PI3K: more than just another effector pathway. Genes Cancer 2, 261–274. [PubMed: 21779497]

Chandra A, Grecco HE, Pisupati V, Perera D, Cassidy L, Skoulidis F, Ismail SA, Hedberg C, Hanzal-Bayer M, Venkitaraman AR, et al. (2011). The GDI-like solubilizing factor PDEδ sustains the spatial organization and signalling of Ras family proteins. Nat. Cell Biol 14, 148–158. [PubMed: 22179043]

Chattopadhyaya R, Meador WE, Means AR, and Quiocho FA (1992). Calmodulin structure refined at 1.7 A resolution. J. Mol. Biol 228, 1177–1192. [PubMed: 1474585]

Chavan TS, Abraham S, and Gaponenko V (2013). Application of reductive ^{13}C-methylation of lysines to enhance the sensitivity of conventional NMR methods. Molecules 18, 7103–7119. [PubMed: 23778120]

Chavan TS, Jang H, Khavrutskii L, Abraham SJ, Banerjee A, Freed BC, Johannessen L, Tarasov SG, Gaponenko V, Nussinov R, et al. (2015). High-affinity interaction of the K-Ras4B hypervariable region with the ras active site. Biophys. J 109, 2602–2613. [PubMed: 26682817]

Delaglio F, Grzesiek S, Vuister GW, Zhu G, Pfeifer J, and Bax A (1995). NMRPipe: a multidimensional spectral processing system based on UNIX pipes. J. Biomol. NMR 6, 277–293. [PubMed: 8520220]

DeLano WL (2002). The PyMOL Molecular Graphics System, Version 1.8 (Schrodinger, LLC).

Deng W, Putkey JA, and Li R (2013). Calmodulin adopts an extended conformation when interacting with L-selectin in membranes. PLoS One 8, e62861. [PubMed: 23658780]

Dharmaiah S, Bindu L, Tran TH, Gillette WK, Frank PH, Ghirlando R, Nissley DV, Esposito D, McCormick F, Stephen AG, et al. (2016). Structural basis of recognition of farnesylated and methylated KRAS4b by PDEdelta. Proc. Natl. Acad. Sci. U S A 113, E6766–E6775. [PubMed: 27791178]

Erwin N, Patra S, and Winter R (2016). Probing conformational and functional substates of calmodulin by high pressure FTIR spectroscopy: influence of Ca^{2+} binding and the hypervariable region of K-Ras4B. Phys. Chem. Chem. Phys 18, 30020–30028. [PubMed: 27774533]

Fivaz M, and Meyer T (2005). Reversible intracellular translocation of KRas but not HRas in hippocampal neurons regulated by Ca^{2+}/calmodulin. J. Cell Biol 170, 429–441. [PubMed: 16043511]

Gifford JL, Ishida H, and Vogel HJ (2012). Structural insights into calmodulin-regulated L-selectin ectodomain shedding. J. Biol. Chem 287, 26513–26527. [PubMed: 22711531]

Gillette WK, Esposito D, Abreu Blanco M, Alexander P, Bindu L, Bittner C, Chertov O, Frank PH, Grose C, Jones JE, et al. (2015). Farnesylated and methylated KRAS4b: high yield production of protein suitable for biophysical studies of prenylated protein-lipid interactions. Sci. Rep 5, 15916. [PubMed: 26522388]

Im W, Lee MS, and Brooks CL 3rd (2003). Generalized born model with a simple smoothing function. J. Comput. Chem 24, 1691–1702. [PubMed: 12964188]

Jang H, Abraham SJ, Chavan TS, Hitchinson B, Khavrutskii L, Tarasova NI, Nussinov R, and Gaponenko V (2015). Mechanisms of membrane binding of small GTPase K-Ras4B farnesylated hypervariable region. J. Biol. Chem 290, 9465–9477. [PubMed: 25713064]

Jang H, Banerjee A, Chavan T, Gaponenko V, and Nussinov R (2017). Flexible-body motions of calmodulin and the farnesylated hypervariable region yield a high-affinity interaction enabling K-Ras4B membrane extraction. J. Biol. Chem 292, 12544–12559. [PubMed: 28623230]

Jang H, Banerjee A, Chavan TS, Lu S, Zhang J, Gaponenko V, and Nussinov R (2016a). The higher level of complexity of K-Ras4B activation at the membrane. FASEB J. 30, 1643–1655. [PubMed: 26718888]

Jang H, Muratcioglu S, Gursoy A, Keskin O, and Nussinov R (2016b). Membrane-associated Ras dimers are isoform-specific: K-Ras dimers differ from H-Ras dimers. Biochem. J 473, 1719–1732. [PubMed: 27057007]

Joyal JL, Burks DJ, Pons S, Matter WF, Vlahos CJ, White MF, and Sacks DB (1997). Calmodulin activates phosphatidylinositol 3-kinase. J. Biol. Chem 272, 28183–28186. [PubMed: 9353264]

Kahraman A, Herzog F, Leitner A, Rosenberger G, Aebersold R, and Malmstrom L (2013). Cross-link guided molecular modeling with ROSETTA. PLoS One 8, e73411. [PubMed: 24069194]

Killock DJ, Parsons M, Zarrouk M, Ameer-Beg SM, Ridley AJ, Haskard DO, Zvelebil M, and Ivetic A (2009). In vitro and in vivo characterization of molecular interactions between calmodulin, Ezrin/Radixin/Moesin, and L-selectin. J. Biol. Chem 284, 8833–8845. [PubMed: 19129194]

Komeiji Y, Ueno Y, and Uebayasi M (2002). Molecular dynamics simulations revealed Ca^{2+}-dependent conformational change of calmodulin. FEBS Lett. 521, 133–139. [PubMed: 12067741]

Lemoine NR, Hughes CM, Barton CM, Poulsom R, Jeffery RE, Kloppel G, Hall PA, and Gullick WJ (1992). The epidermal growth factor receptor in human pancreatic cancer. J. Pathol 166, 7–12. [PubMed: 1538276]

Liao J, Planchon SM, Wolfman JC, and Wolfman A (2006). Growth factor-dependent AKT activation and cell migration requires the function of c-K(B)-Ras versus other cellular ras isoforms. J. Biol. Chem 281, 29730–29738. [PubMed: 16908523]

Liao TJ, Jang H, Fushman D, and Nussinov R (2018). Allosteric KRas4B can modulate SOS1 fast and slow Ras activation cycles. Biophys. J 115, 629–641. [PubMed: 30097175]

Logothetis DE, Petrou VI, Zhang M, Mahajan R, Meng XY, Adney SK, Cui M, and Baki L (2015). Phosphoinositide control of membrane protein function: a frontier led by studies on ion channels. Annu. Rev. Physiol 77, 81–104. [PubMed: 25293526]

Lopez-Alcala C, Alvarez-Moya B, Villalonga P, Calvo M, Bachs O, and Agell N (2008). Identification of essential interacting elements in K-Ras/calmodulin binding and its role in K-Ras localization. J. Biol. Chem 283, 10621–10631. [PubMed: 18182391]

Lu S, Banerjee A, Jang H, Zhang J, Gaponenko V, and Nussinov R (2015). GTP binding and oncogenic mutations may attenuate hypervariable region (HVR)-catalytic domain interactions in small GTPase K-Ras4B, exposing the effector binding site. J. Biol. Chem 290, 28887–28900. [PubMed: 26453300]

Lu S, Jang H, Nussinov R, and Zhang J (2016). The structural basis of oncogenic mutations G12, G13 and Q61 in small GTPase K-Ras4B. Sci. Rep 6, 21949. [PubMed: 26902995]

Matsubara M, Nakatsu T, Kato H, and Taniguchi H (2004). Crystal structure of a myristoylated CAP-23/NAP-22 N-terminal domain complexed with Ca^{2+}/calmodulin. EMBO J. 23, 712–718. [PubMed: 14765114]

Meador WE, Means AR, and Quiocho FA (1992). Target enzyme recognition by calmodulin: 2.4 Å structure of a calmodulin-peptide complex. Science 257, 1251–1255. [PubMed: 1519061]

Muratcioglu S, Jang H, Gursoy A, Keskin O, and Nussinov R (2017). PDEdelta binding to ras isoforms provides a route to proper membrane localization. J. Phys. Chem. B 121, 5917–5927. [PubMed: 28540724]

Nolte RT, Eck MJ, Schlessinger J, Shoelson SE, and Harrison SC (1996). Crystal structure of the PI 3-kinase p85 amino-terminal SH2 domain and its phosphopeptide complexes. Nat. Struct. Biol 3, 364–374. [PubMed: 8599763]

Nussinov R, Muratcioglu S, Tsai CJ, Jang H, Gursoy A, and Keskin O (2015). The key role of calmodulin in KRAS-driven adenocarcinomas. Mol. Cancer Res 13, 1265–1273. [PubMed: 26085527]

Nussinov R, Muratcioglu S, Tsai CJ, Jang H, Gursoy A, and Keskin O (2016a). K-Ras4B/calmodulin/PI3Kα: a promising new adenocarcinoma-specific drug target? Expert Opin. Ther. Targets 20, 831–842. [PubMed: 26873344]

Nussinov R, Tsai CJ, Chakrabarti M, and Jang H (2016b). A new view of Ras isoforms in cancers. Cancer Res. 76, 18–23. [PubMed: 26659836]

Nussinov R, Tsai CJ, and Jang H (2019a). Is nanoclustering essential for all oncogenic KRas pathways? Can it explain why wild-type KRas can inhibit its oncogenic variant? Semin. Cancer Biol 54, 114–120. [PubMed: 29307569]

Nussinov R, Tsai CJ, and Jang H (2019b). Oncogenic KRas mobility in the membrane and signaling response. Semin. Cancer Biol 54, 109–113. [PubMed: 29499269]

Nussinov R, Tsai CJ, Jang H, Korcsmaros T, and Csermely P (2016c). Oncogenic KRAS signaling and YAP1/βs-catenin: similar cell cycle control in tumor initiation. Semin. Cell Dev. Biol 58, 79–85. [PubMed: 27058752]

Nussinov R, Zhang M, Tsai CJ, and Jang H (2018a). Calmodulin and IQGAP1 activation of PI3Kalpha and Akt in KRAS, HRAS and NRAS-driven cancers. Biochim. Biophys. Acta Mol. Basis Dis 1864, 2304–2314. [PubMed: 29097261]

Nussinov R, Zhang M, Tsai CJ, Liao TJ, Fushman D, and Jang H (2018b). Autoinhibition in Ras effectors Raf, PI3Kalpha, and RASSF5: a comprehensive review underscoring the challenges in pharmacological intervention. Biophys. Rev 10, 1263–1282. [PubMed: 30269291]

Oliveira-Cunha M, Newman WG, and Siriwardena AK (2011). Epidermal growth factor receptor in pancreatic cancer. Cancers (Basel) 3, 1513–1526. [PubMed: 24212772]

Ozdemir ES, Jang H, Gursoy A, Keskin O, Li Z, Sacks DB, and Nussinov R (2018a). Unraveling the molecular mechanism of interactions of the Rho GTPases Cdc42 and Rac1 with the scaffolding protein IQGAP2. J. Biol. Chem 293, 3685–3699. [PubMed: 29358323]

Ozdemir ES, Jang H, Gursoy A, Keskin O, and Nussinov R (2018b). Arl2-mediated allosteric release of farnesylated KRas4B from shuttling factor PDEdelta. J. Phys. Chem. B 122, 7503–7513. [PubMed: 29961325]

Parker JA, Volmar AY, Pavlopoulos S, and Mattos C (2018). K-Ras populates conformational states differently from its isoform H-ras and oncogenic mutant K-RasG12D. Structure 26, 810–820.e4. [PubMed: 29706533]

Pauptit RA, Dennis CA, Derbyshire DJ, Breeze AL, Weston SA, Rowsell S, and Murshudov GN (2001). NMR trial models: experiences with the colicin immunity protein Im7 and the p85alpha C-terminal SH2-peptide complex. Acta Crystallogr. D Biol. Crystallogr 57, 1397–1404. [PubMed: 11567151]

Pelikan M, Hura GL, and Hammel M (2009). Structure and flexibility within proteins as identified through small angle X-ray scattering. Gen. Physiol. Biophys 28, 174–189.

Pettersen EF, Goddard TD, Huang CC, Couch GS, Greenblatt DM, Meng EC, and Ferrin TE (2004). UCSF Chimera—a visualization system for exploratory research and analysis. J. Comput. Chem 25, 1605–1612. [PubMed: 15264254]

Phillips JC, Braun R, Wang W, Gumbart J, Tajkhorshid E, Villa E, Chipot C, Skeel RD, Kale L, and Schulten K (2005). Scalable molecular dynamics with NAMD. J. Comput. Chem 26, 1781–1802. [PubMed: 16222654]

Rodi DJ, Mandava S, Gore DB, Makowski L, and Fischetti RF (2007). Detection of functional ligand-binding events using synchrotron X-ray scattering. J. Biomol. Screen 12, 994–998. [PubMed: 17942792]

Sauter DRP, Novak I, Pedersen SF, Larsen EH, and Hoffmann EK (2015). ANO1 (TMEM16A) in pancreatic ductal adenocarcinoma (PDAC). Pflugers Arch. 467, 1495–1508. [PubMed: 25163766]

Schmick M, Vartak N, Papke B, Kovacevic M, Truxius DC, Rossmannek L, and Bastiaens PI (2014). KRas localizes to the plasma membrane by spatial cycles of solubilization, trapping and vesicular transport. Cell 157, 459–471. [PubMed: 24725411]

Schneidman-Duhovny D, Hammel M, Tainer JA, and Sali A (2016). FoXS, FoXSDock and MultiFoXS: single-state and multi-state structural modeling of proteins and their complexes based on SAXS profiles. Nucleic Acids Res. 44, W424–W429. [PubMed: 27151198]

Sidhu RS, Clough RR, and Bhullar RP (2003). Ca^{2+}/calmodulin binds and dissociates K-RasB from membrane. Biochem. Biophys. Res. Commun 304, 655–660. [PubMed: 12727204]

Sircar A, Chaudhury S, Kilambi KP, Berrondo M, and Gray JJ (2010). A generalized approach to sampling backbone conformations with RosettaDock for CAPRI rounds 13-19. Proteins 78, 3115–3123. [PubMed: 20535822]

Sperlich B, Kapoor S, Waldmann H, Winter R, and Weise K (2016). Regulation of K-Ras4B membrane binding by calmodulin. Biophys. J 111, 113–122. [PubMed: 27410739]

Stevens FC (1983). Calmodulin: an introduction. Can. J. Biochem. Cell Biol 61, 906–910. [PubMed: 6313166]

Villalonga P, Lopez-Alcala C, Bosch M, Chiloeches A, Rocamora N, Gil J, Marais R, Marshall CJ, Bachs O, and Agell N (2001). Calmodulin binds to K-Ras, but not to H- or N-Ras, and modulates its downstream signaling. Mol. Cell Biol 21, 7345–7354. [PubMed: 11585916]

Wang G, Zhang M, Jang H, Lu S, Lin S, Chen G, Nussinov R, Zhang J, and Gaponenko V (2018). Interaction of calmodulin with the cSH2 domain of the p85 regulatory subunit. Biochemistry 57, 1917–1928. [PubMed: 29494137]

Wang MT, Holderfield M, Galeas J, Delrosario R, To MD, Balmain A, and McCormick F (2015). K-Ras promotes tumorigenicity through suppression of non-canonical Wnt signaling. Cell 163, 1237–1251. [PubMed: 26590425]

Weise K, Kapoor S, Werkmuller A, Mobitz S, Zimmermann G, Triola G, Waldmann H, and Winter R (2012). Dissociation of the K-Ras4B/PDEδ complex upon contact with lipid membranes: membrane delivery instead of extraction. J. Am. Chem. Soc 134, 11503–11510. [PubMed: 22721555]

Wu LJ, Xu LR, Liao JM, Chen J, and Liang Y (2011). Both the C-terminal polylysine region and the farnesylation of K-RasB are important for its specific interaction with calmodulin. PLoS One 6, e21929. [PubMed: 21750741]

Yamauchi E, Nakatsu T, Matsubara M, Kato H, and Taniguchi H (2003). Crystal structure of a MARCKS peptide containing the calmodulin-binding domain in complex with Ca^{2+}-calmodulin. Nat. Struct. Biol 10, 226–231. [PubMed: 12577052]

Yu J, Wjasow C, and Backer JM (1998). Regulation of the p85/p110alpha phosphatidylinositol 3'-kinase. Distinct roles for the N-terminal and C-terminal SH2 domains. J. Biol. Chem 273, 30199–30203. [PubMed: 9804776]

Zhang M, Jang H, Gaponenko V, and Nussinov R (2017). Phosphorylated calmodulin promotes PI3K activation by binding to the SH2 domains. Biophys. J 113, 1956–1967. [PubMed: 29117520]

Zhang M, Jang H, and Nussinov R (2019a). The mechanism of PI3Kα activation at the atomic level. Chem. Sci 10, 3671–3680. [PubMed: 30996962]

Zhang M, Jang H, and Nussinov R (2019b). The structural basis for Ras activation of PI3Kα lipid kinase. Phys. Chem. Chem. Phys 21, 12021–12028. [PubMed: 31135801]

Zhang M, Li Z, Wang G, Jang H, Sacks DB, Zhang J, Gaponenko V, and Nussinov R (2018). Calmodulin (CaM) activates PI3Kalpha by targeting the "Soft" CaM-binding motifs in both the nSH2 and cSH2 domains of p85alpha. J. Phys. Chem. B 122, 11137–11146. [PubMed: 30047727]

Zhang M, Meng XY, Cui M, Pascal JM, Logothetis DE, and Zhang JF (2014). Selective phosphorylation modulates the PIP2 sensitivity of the CaM-SK channel complex. Nat. Chem. Biol 10, 753–759. [PubMed: 25108821]

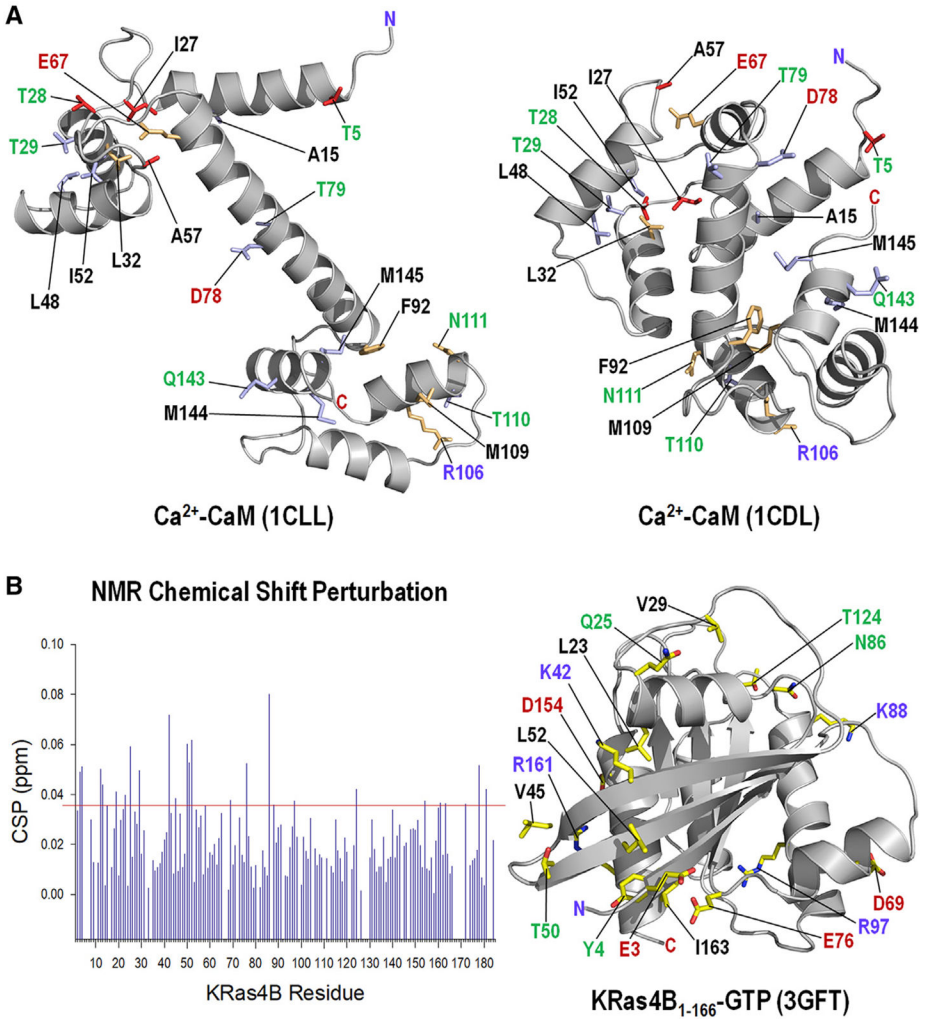

Figure 1. NMR CSPs and Mapping on the Structure

(A) NMR CSPs of residues by truncated KRas4B$_{1\text{-}166}$ (red sticks) and by full-length KRas4B$_{1\text{-}188}$ (light blue sticks) mapped onto the crystal structures of CaM with a stretched central linker (PDB: 1CLL) (left panel) and a collapsed linker (PDB: 1CDL) (right panel). The light green sticks denote the perturbed residues by both truncated and full-length KRas4B.

(B) NMR CSPs of residues in full-length KRas4B$_{1\text{-}188}$ in the GTP-γ-S bound state by CaM (left panel), and mapping of the perturbed residues on the crystal structure (PDB: 3GFT) of the catalytic domain of KRas4B (right panel). In the structure, hydrophobic, hydrophilic, positively charged, and negatively charged residues are marked by black, green, blue, and red letters, respectively.

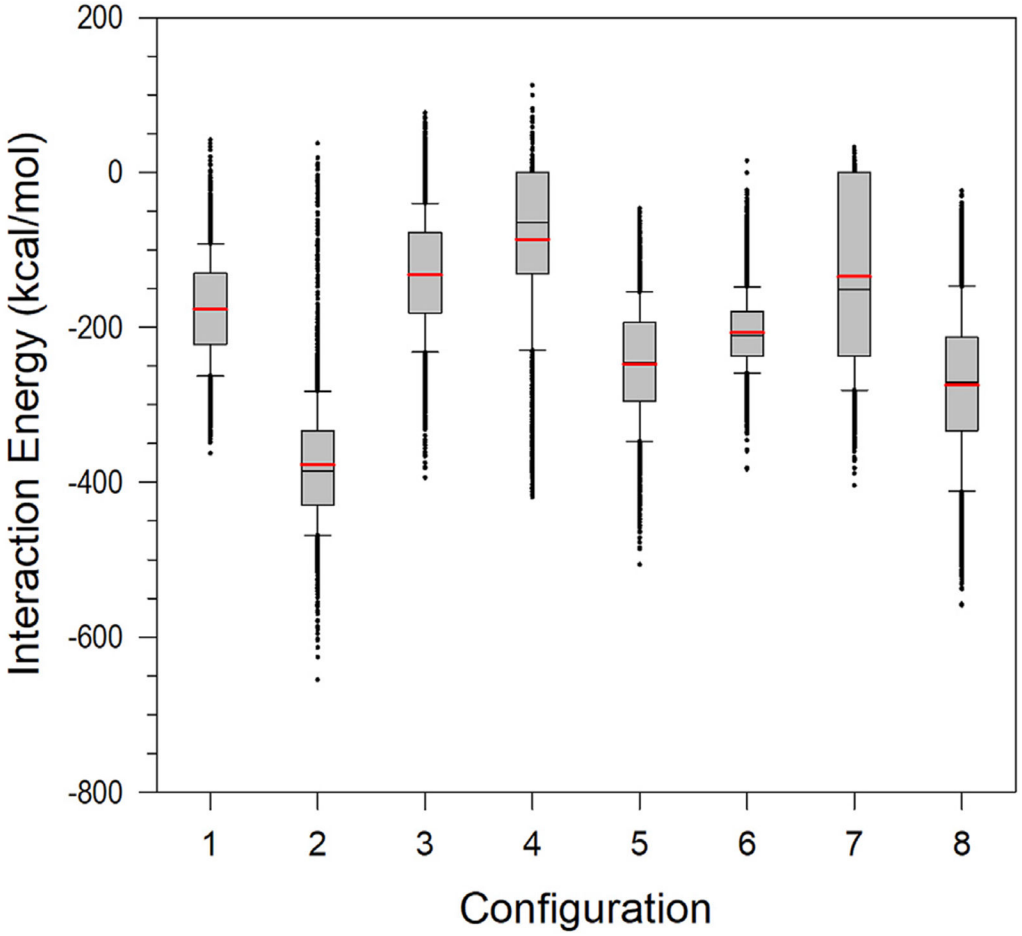

Figure 2. Averaged Total Interaction Energies of Truncated KRas4B$_{1\text{-}166}$ with CaM

In the box graphs, the red and black lines denote the mean and median values, respectively. Whiskers above and below the box denote the 90th and 10th percentiles.

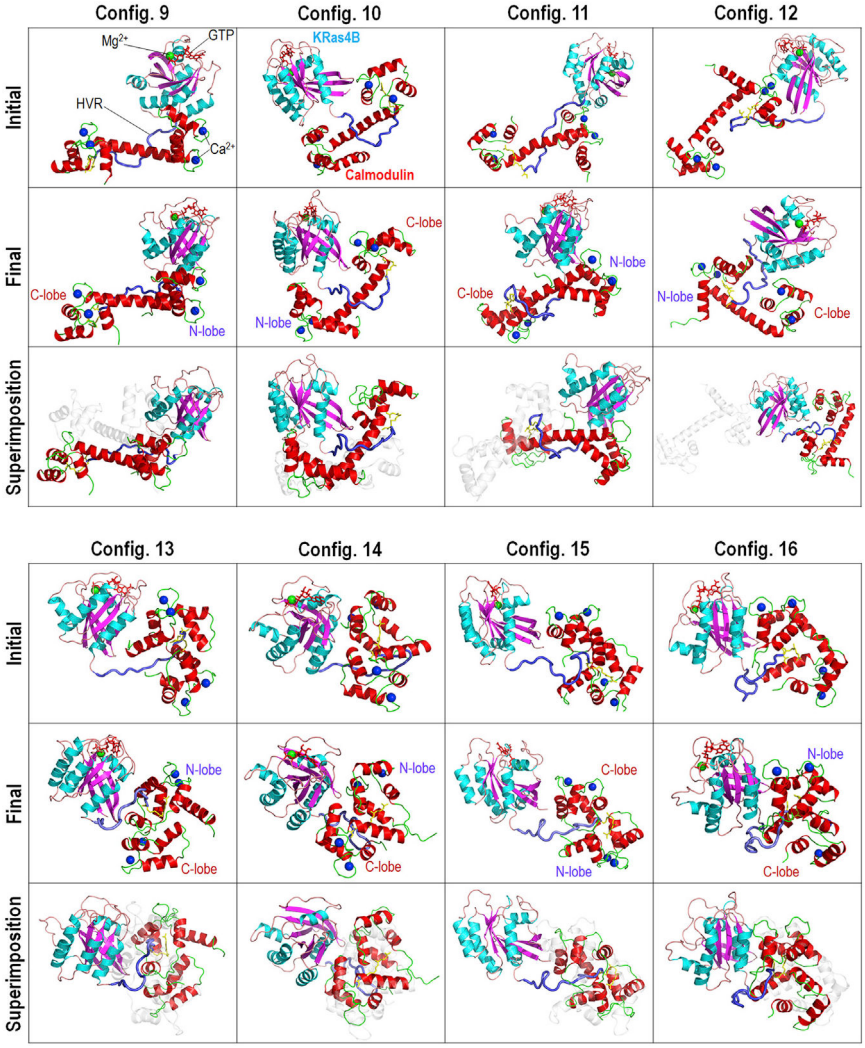

Figure 3. Simulated Configurations of KRas4B$_{1\text{-}185}$-CaM Complex

Snapshots representing the initial (upper panel of each configuration), final (middle panel of each configuration), and superimposition of the initial and final structures (lower panel of each configuration) for the FME KRas4B$_{1\text{-}185}$-CaM complex. In the superimpositions, initial structures are shown as white transparent cartoons.

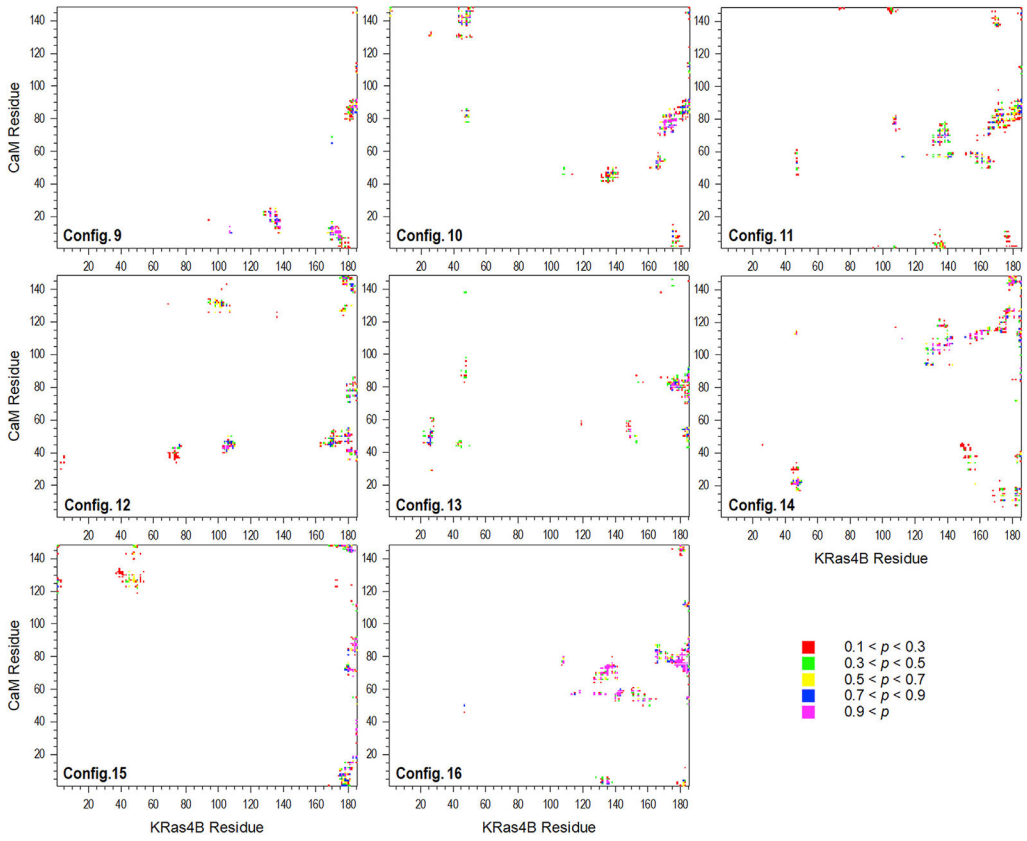

Figure 4. Intermolecular Residue-Residue Contacts Between FME KRas4B$_{1\text{-}185}$ and CaM

For two intermolecular residues *i* and *j*, the probability of contact for the distance between the C_{β}^{i} – C_{β}^{j} atom (C_{α} is used for Gly residue) with cutoff 10 Å was calculated.

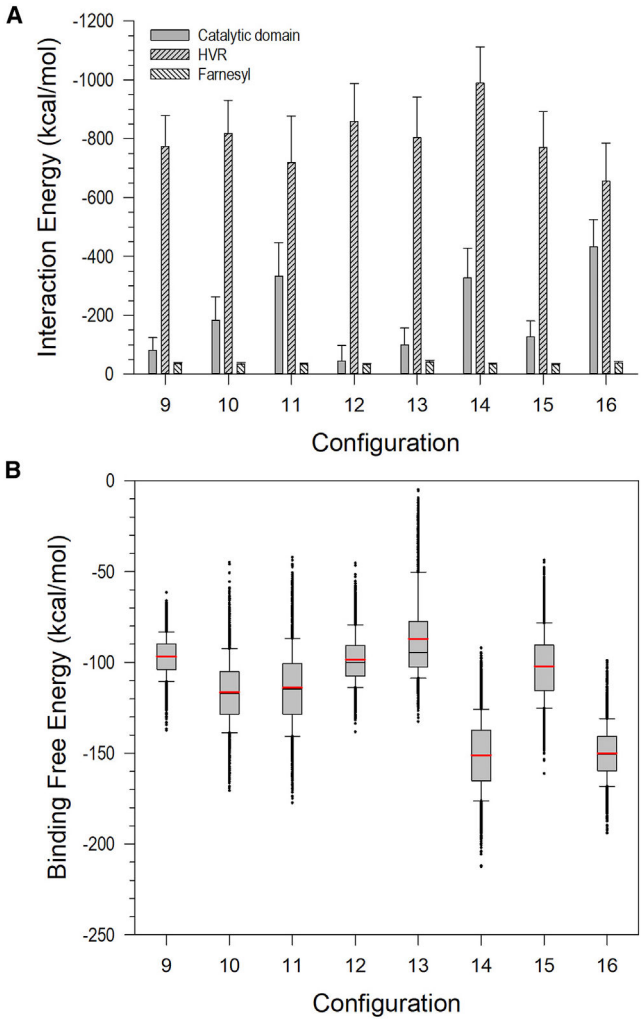

Figure 5. Interaction Energy and Binding Free Energy

(A) Averaged interaction energies of the catalytic domain, HVR, and farnesyl of FME KRas4B$_{1\text{-}185}$ with CaM. Error bars indicate standard deviation.

(B) Binding free energy for the FME KRas4B$_{1\text{-}185}$ interaction with CaM. In the calculation, gas phase contribution, the solvation energy contribution, and the entropic contribution combines the average binding free energy. In the box graphs, the red and black lines denote the mean and median values, respectively. Whiskers above and below the box denote the 90th and 10th percentiles.

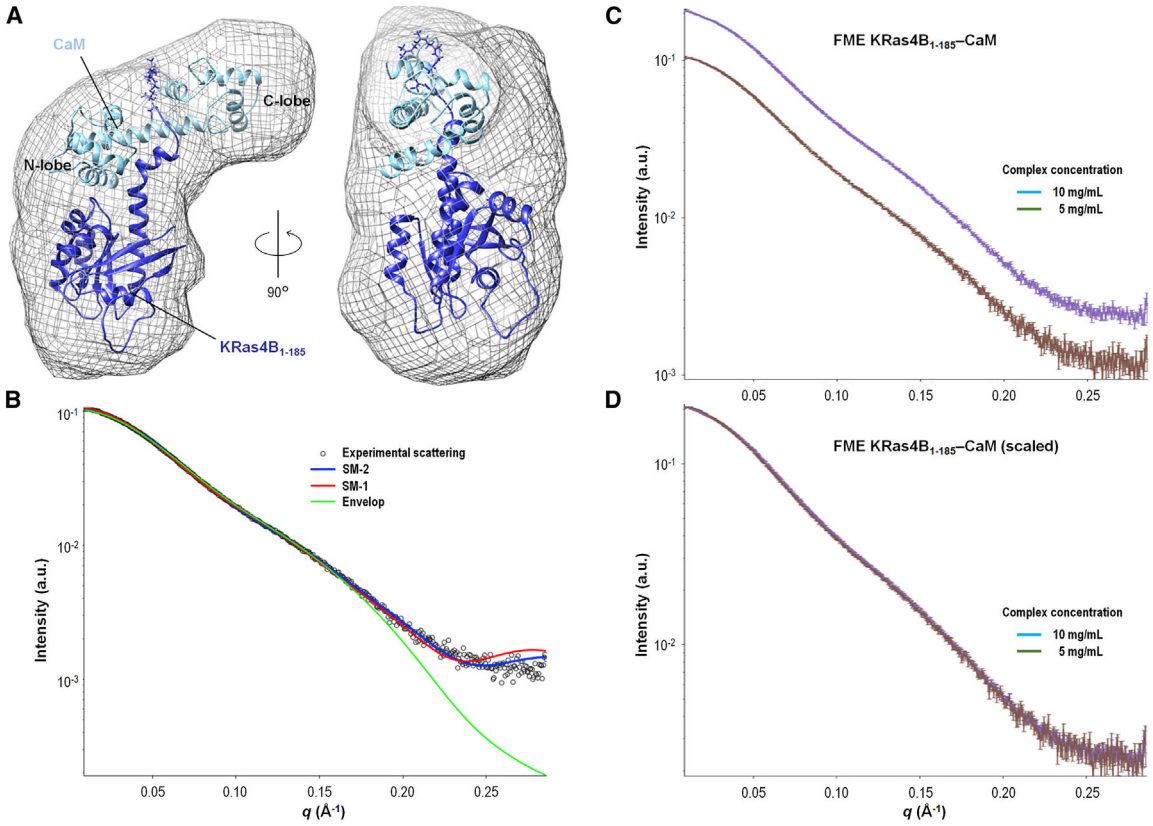

Figure 6. SAXS Model 2 of KRas4B-CaM Complex

(A) Proposed SAXS model 2 (SM-2) of the $KRas4B_{1\text{-}185}$-CaM complex. An averaged *ab initio* model constructed from the SAXS data is superimposed with the proposed model of FME $KRas4B_{1\text{-}185}$-GppNHp (dark blue) in complex with CaM (light blue).

(B) The SAXS data (open circles) are plotted with the theoretical scattering curves of the envelope (green), SM-1 (red), and SM-2 (blue). The fit of SM-2 ($\chi^2 = 1.84$) against the experimental data is significantly better than those for SM-1 ($\chi^2 = 2.14$) or the envelope ($\chi^2 > 3$).

(C) The SAXS data are plotted with explicit error for two concentrations of FME $KRas4B_{1\text{-}185}$-CaM samples (5 mg/mL, brown, and 10 mg/mL, purple). The experimental scattering curves between the two samples are nearly identical.

(D) The SAXS of the two samples are plotted, with a scaling factor of 1.98 applied to the 5 mg/mL data. The scaling of the 5 mg/mL data by a factor of nearly 2 for optimal alignment with the 10 mg/mL scattering curve suggests that the concentrations of the complexes were correctly characterized, with no protein aggregation. The two curves superimpose well with the same features, indicating that the two samples contain the same species.

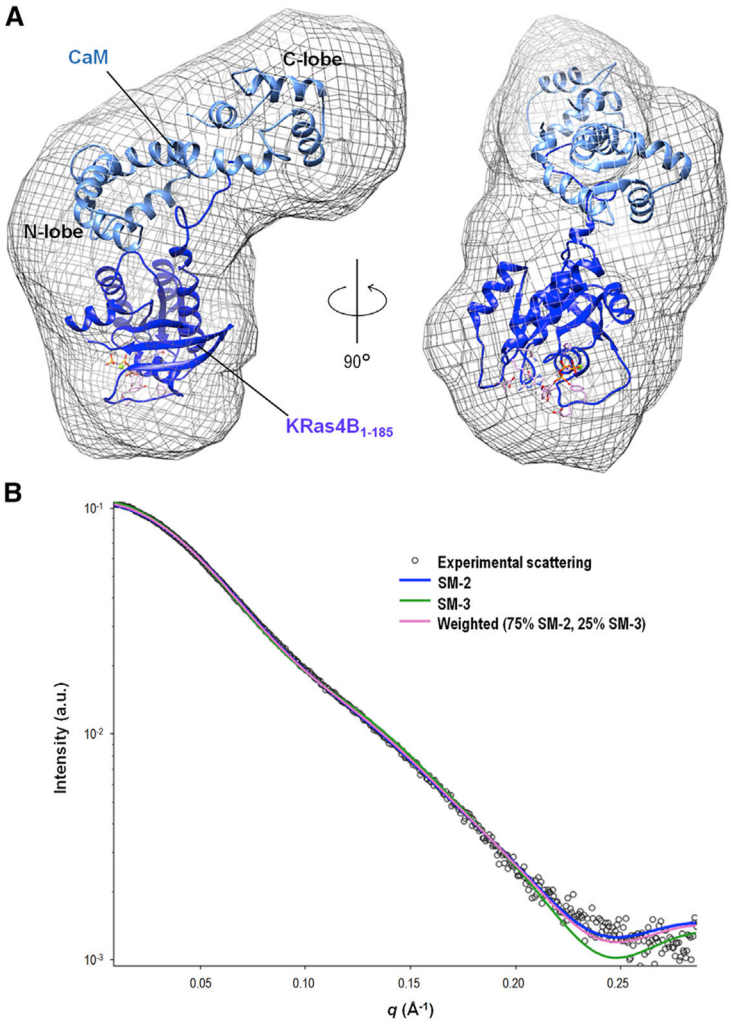

Figure 7. SAXS Model 3 of KRas4B-CaM Complex

(A) Proposed SAXS model 3 (SM-3) of the $KRas4B_{1-185}$-CaM complex. SM-3 was aligned within the calculated envelope of FME $KRas4B_{1-185}$-GppNHp SAXS data. The hybrid model of full-length $KRas4B_{1-185}$ (dark blue) and CaM (light blue) is shown in the SAXS envelope.

(B) The experimental SAXS data (open circles) is plotted with theoretical scattering of SM-3 (green, $\chi^2 = 2.12$), and a weighed theoretical scattering of SM-3 (25%) and SM-2 (75%) (pink, $\chi^2 = 1.65$). The theoretical scattering of SM-2 (blue) is also plotted for comparison. Weighing calculations were performed in MultiFoXS (Schneidman-Duhovny et al., 2016).

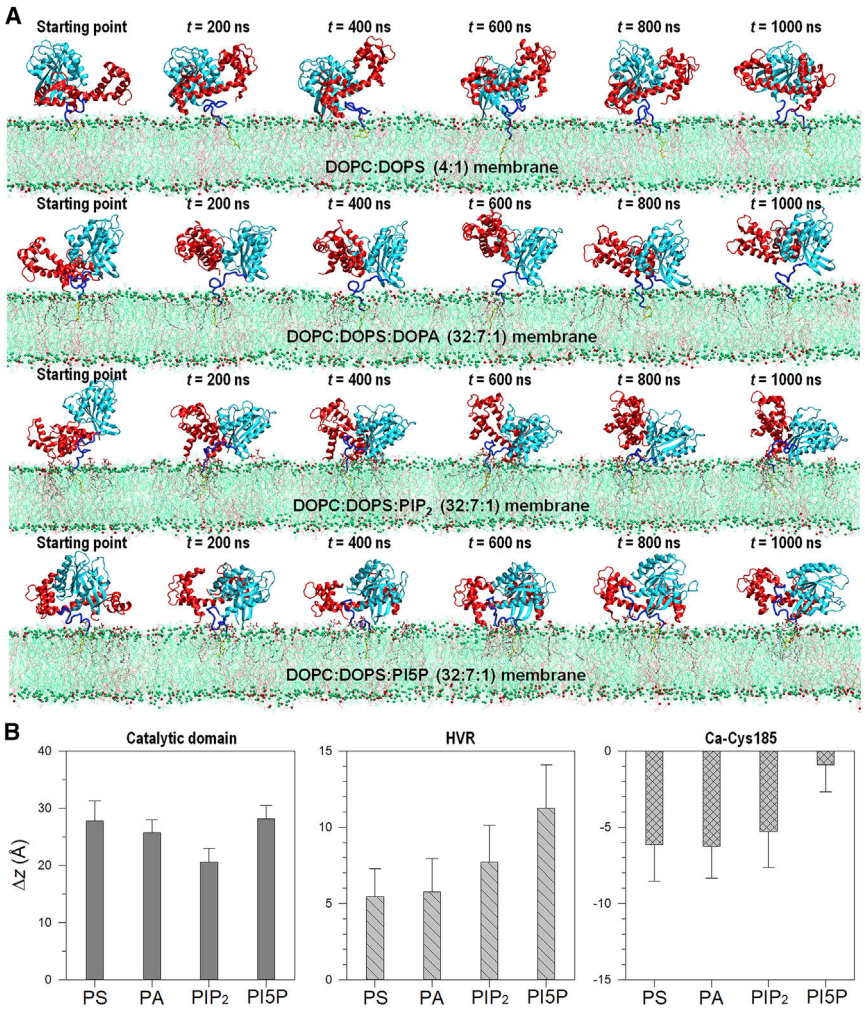

Figure 8. KRas4B Interaction with CaM at the Membrane

(A) Time-series of snapshots of FME KRas4B$_{1\text{-}185}$ interacting with CaM at the anionic lipid bilayers composed of DOPC:DOPS (molar ratio 4:1), DOPC:DOPS:DOPA (molar ratio 32:7:1), DOPC: DOPS:PIP$_2$ (molar ratio 32:7:1), and DOPC:DOPS: PI5P (molar ratio 32:7:1) lipids in the liquid phase. In the cartoons, the KRas4B catalytic domain, HVR, and farnesyl are shown in light blue, dark blue, and yellow, respectively, and CaM is shown in red.

(B) The deviation, Δz, from the averaged phosphate atoms position at the upper bilayer leaflet for the center of mass of the KRas4B catalytic domain (left panel), HVR (middle panel), and CA atom of Cys185 (right panel) at the anionic PS, PA, PIP$_2$, and PI5P bilayers. The location of the bilayer surface can be defined +5 Å from $\Delta z = 0$. Error bars indicate standard deviation.

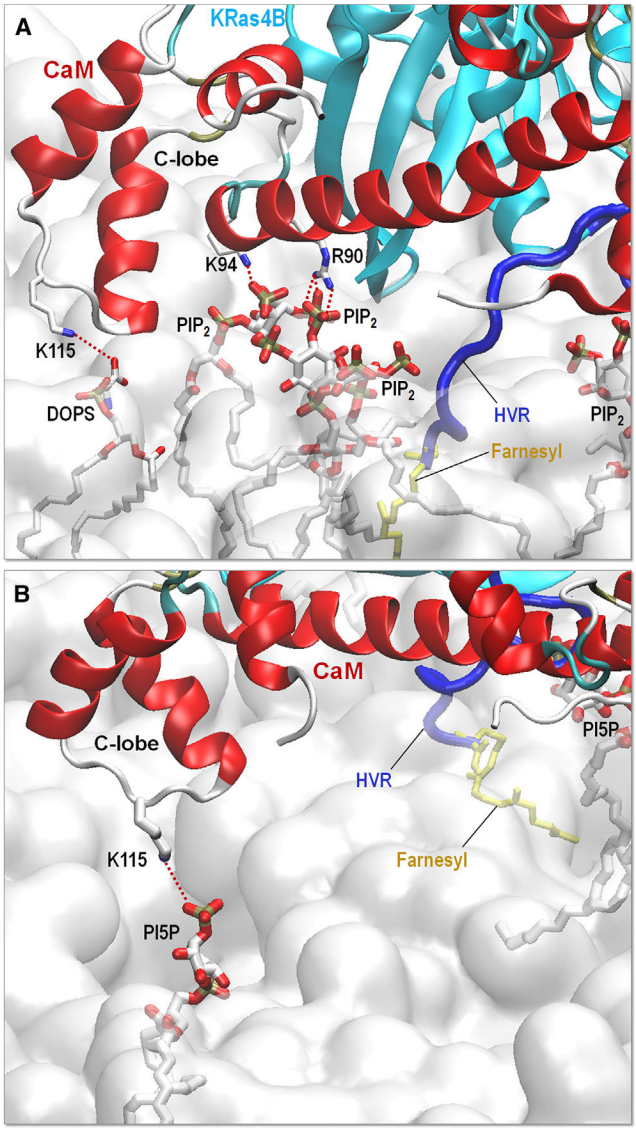

Figure 9. CaM Interaction with Signaling Lipids

Snapshots depicting the interaction of CaM with signaling lipids at the (A) PIP_2 (DOPC:DOPS:PIP_2 with molar ratio 32:7:1) and (B) PI5P (DOPC:DOPS:PI5P with molar ratio 32:7:1) bilayers. Red dotted lines highlight the salt bridge interaction.

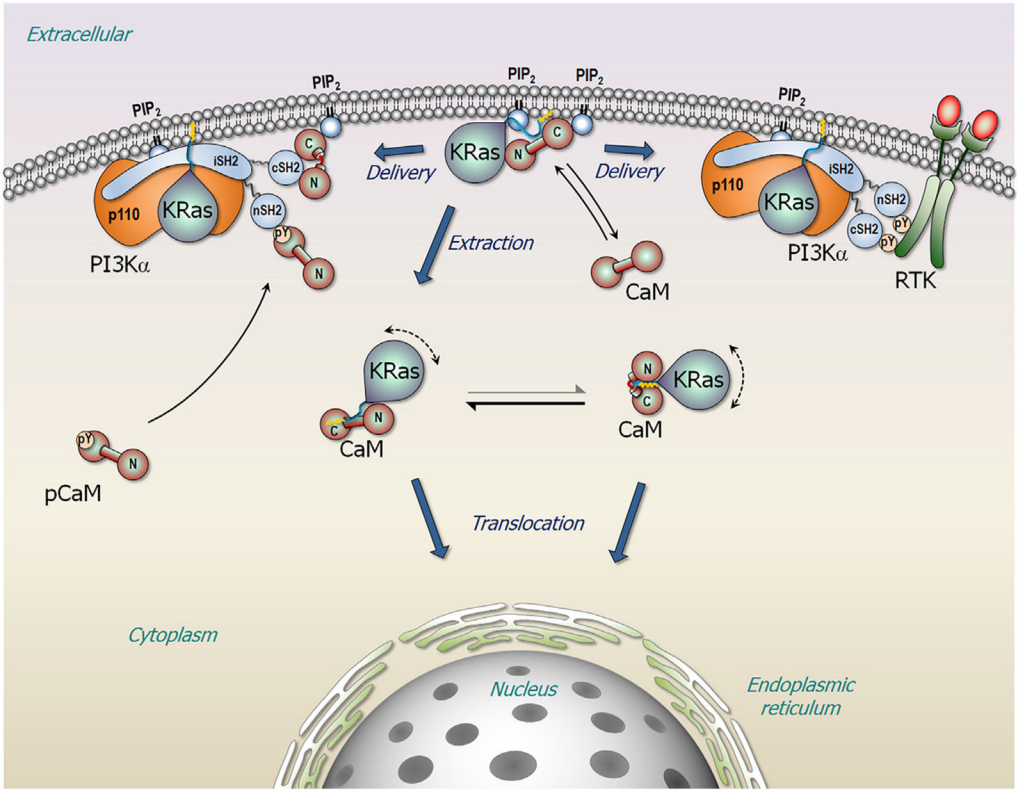

Figure 10. A Schematic Diagram Illustrating the Role of KRas4B and CaM in Promoting PI3Kα Activation

CaM extracts KRas4B from the plasma membrane for intracellular translocation. Signaling lipids, such as PIP_2 and PI5P may prevent the event, constraining the complex at the membrane. In *KRAS*-driven adenocarcinoma, the KRas4B-CaM complex recruits PI3Kα to the membrane, substituting the missing RTK signal.

KEY RESOURCES TABLE

REAGENT or RESOURCE	SOURCE	IDENTIFIER
Biological Samples		
cDNA for Chicken CaM	Prof. Joshua Wand	N/A
FME KRas4B bound to GppNHp	NCI Ras initiative team	N/A
Deposited Data		
Crystal structure of CaM with extended linker	Chattopadhyaya et al., 1992	PDB: 1CLL
Crystal structure of CaM with collapsed linker in complex with MYLK peptide	Meador et al., 1992	PDB: 1CDL
Crystal structure of CaM with extended linker	Babu et al., 1988	PDB: 3CLN
Crystal structure of KRas4B	https://doi.org/10.2210/pdb3GFT/pdb	PDB: 3GFT
Crystal structure of KRas4B in complex with PDEδ	Dharmaiah et al., 2016	PDB: 5TAR
Crystal structure of KRas4B	Parker et al., 2018	PDB: 5UK9
Experimental Models: Cell Lines		
BL21(DE3)	This paper	N/A
Software and Algorithms		
Rosetta docking program	(Kahraman et al., 2013; Sircar et al., 2010)	https://www.rosettacommons.org/software
CHARMM programming package	(Brooks et al., 2009)	https://www.charmm.org/
NAMD 2.12	(Phillips et al., 2005)	http://www.ks.uiuc.edu/Research/namd/
The ATSAS program	Cornell High Energy Synchrotron Source (CHESS) at Cornell University (Ithaca, NY)	https://www.chess.cornell.edu/
PyMOL	(DeLano, 2002)	https://pymol.org/2/
Chimera	(Pettersen et al., 2004)	https://www.cgl.ucsf.edu/chimera/
FoXS and MultiFoXS programs	(Pelikan et al., 2009; Schneidman-Duhovny et al., 2016)	https://modbase.compbio.ucsf.edu/modbase-cgi/index.cgi